

Correlations between turbulent velocity and density fields in the local interstellar medium

P. M. W. Kalberla¹, J. Kerp¹ and U. Haud²

¹ Argelander-Institut für Astronomie, Auf dem Hügel 71, 53121 Bonn, Germany
e-mail: pkalberla@astro.uni-bonn.de

² Tartu Observatory, University of Tartu, 61602 Tõravere, Tartumaa, Estonia

Received 17 September 2021 / Accepted 26 January 2022

ABSTRACT

Context. Turbulence is expected to generate characteristic velocity and density fluctuations in the interstellar medium (ISM).

Aims. Using H I survey data, we distinguish these contributions as the basis of comparisons with theoretical and magnetohydrodynamical (MHD) simulations.

Methods. We used HI4PI multiphase observations and Gaussian components representing three H I phases, the cold, warm, and unstable lukewarm medium (CNM, WNM and LNM, respectively) to deduce characteristic fluctuations in turbulent density and velocity fields. We applied the velocity decomposition algorithm (VDA) for separating such fluctuations in the position-position-velocity (PPV) space.

Results. The VDA extends the velocity channel analysis (VCA) by Lazarian and Pogosyan and predicts that turbulent velocity and density fields are statistically uncorrelated. Multiphase MHD simulations of turbulent flows in the ISM are consistent with this proposal. Applying the VDA decomposition to the observational data (here, HI4PI) yields – contrary to our expectations – a significant correlation between velocity and density fields. All H I phases contribute to this correlation. The correlations in the velocity wings suffer from attenuation caused by uncorrelated noise. Both VCA and VDA predict that dispersions from fluctuations in narrow velocity channels scale in proportion to the average intensity. Observed brightness temperature fluctuations follow, however, a square-root scaling – as expected for a sum of normally distributed random sources. Fluctuations in H I channel maps at high spatial frequencies are observed to be dominated by density structures, which is in opposition to the results from MHD simulations, where small-scale structures are predicted to have been generated predominantly by velocity caustics.

Conclusions. The VCA predictions and VDA results on MHD simulations are not compatible with the H I observations. The observed turbulent velocity and density fields in the ISM are not statistically uncorrelated, but they do reveal significant interrelations.

Key words. ISM: clouds – ISM: structure – dust, extinction – turbulence – magnetic fields – magnetohydrodynamics (MHD)

1. Introduction

It is commonly accepted that most processes and structures in the interstellar medium (ISM) are strongly affected by turbulence (e.g., Elmegreen & Scalo 2004), however, the specific details of the turbulent flow remain uncertain. In addition, the interpretation of observed structures, particularly the nature of H I filaments, is still a matter of debate. High-resolution all-sky H I observations of the local ISM have provided a wealth of data that await analysis and the time is right to work out how these data can be interpreted in the presence of current turbulence paradigms.

H I observations are organized in position-position-velocity (PPV) data cubes with a number of channel maps, which are individual slices of intensities in brightness temperature at constant radial velocity. The relation between the statistics of intensity fluctuations within these channel maps and the statistics of the underlying velocity and density distributions is non-trivial and depends on the properties of the turbulent field. The velocity channel analysis (VCA; Lazarian & Pogosyan 2000) provides the necessary tools to disentangle velocity and density effects on observed H I structures. In case of an optically thin medium, it is intuitively clear that the column density distribution, obtained after integrating in velocity along the line of sight, can only be influenced by density fluctuations. In this case, the velocity in-

formation is lost, leading to missed details on the velocity structure of the derived column density features. To recover the velocity information, varying the width of the velocity window is a commonly used approach. To disentangle the statistics of underlying velocity structures, it is necessary to consider the question of whether the eddies under consideration, which are of a particular size and velocity dispersion, fit within the defined velocity window. This is roughly the VCA concept used by Lazarian & Pogosyan (2000) to disentangle the statistics of underlying velocities and densities in the turbulent volume. Intensity fluctuations within individual observed H I channel maps are assumed to be caused by projection effects from velocity crowding of unrelated structures along the line of sight. Observed structures in channel maps are accordingly coming from contributions from components in different physical locations along the line of sight (Lazarian & Yuen 2018). Such contributions to the velocity channels are referred to as velocity caustics.

Contrary to such a statistical description of a turbulent medium, observations suggest that a significant fraction of the intensity structures are related to spatially coherent cloud complexes. Turbulent motions determine the temporal and spatial structure of the thermal pressure (Wolfire et al. 2003, Sect. 2). The velocity dispersion of gaseous structures increases with scale (Larson 1981) but the thermal pressure regulating

phase transitions and phase fractions remains essentially scale-independent (Spitzer 1968; McKee & Ostriker 1977), even though phase transitions can be triggered by turbulence (e.g., Saury et al. 2014). Thus, the basic understanding of a majority of the observers is still that H I structures may be represented by a so-called raisin pudding model (Clark 1965), in which cool and dense clouds (raisins) are embedded in a hot, diffuse intercloud medium. This model was extended to a multiphase medium, including the warm ionized medium (WIM) (McKee & Ostriker 1977) and some amounts of thermal unstable neutral H I, “lukewarm” according to Salpeter (1976). As discussed by Elmegreen & Scalo (2004), most observers have found no compelling evidence to substitute the cloud-intercloud model in favor of one with widespread turbulence. The millennium Arecibo 21 centimeter absorption-line survey (Heiles & Troland 2005) has led to the conclusion that there is a well-defined median magnetic field in the cold neutral medium (CNM) which dominates thermal motions. Turbulence and magnetism are found in approximate equipartition.

Within the last decade, several high resolution large scale H I data bases have become available: the Leiden-Argentine-Bonn (LAB; Kalberla et al. 2005), the Galactic All Sky Survey (GASS; McClure-Griffiths et al. 2009 and Kalberla & Haud 2015), the Effelsberg-Bonn H I Survey (EBHIS; Winkel et al. 2016) and the Galactic Arecibo L-Band Feed Array H I survey (GALFA-H I; Peek et al. 2018). The relations between H I and FIR have been studied in many publications since Boulanger & Perault (1988). Recent high-resolution surveys show a rich wealth of H I filaments in the diffuse ISM (e.g., Clark et al. 2014 or Kalberla et al. 2016) that appear to be aligned preferentially with the magnetic field. These are usually interpreted in terms of density fluctuations (Clark et al. 2015; Miville-Deschênes et al. 2016). Clark & Hensley (2019) report evidence for a coupling of linear density structures in H I and dust to the Galactic magnetic field.

Measuring accurate H I excitation temperatures and densities requires the determination of both emission and absorption, but absorption observations are limited by the availability of continuum background sources (e.g., Heiles & Troland 2005 or Murray et al. 2018). In particular, Murray et al. (2020) approached this problem using deep learning methods. Their results support the scenario that small-scale H I structures aligned with the magnetic field are characteristic for the CNM, supporting the conclusion that real density structures are dominated by the CNM.

Despite several major surveys in emission and absorption that have become available since Lazarian & Pogosyan (2000), the interpretation of filamentary H I and dust structures has remained controversial. The interpretation of filamentary structures as fibers in the sense of coherent density structures (Clark et al. 2014, 2015) was challenged by Lazarian & Yuen (2018). In the framework of VCA, the H I structures seen in individual channel maps are interpreted as velocity caustics, namely, intensity structures created by turbulent velocity fluctuations. The VCA paradigm is that velocity crowding along the line of sight causes the observed intensity enhancements that erroneously are interpreted as density structures. Thus, caustics mimic real physical entities. Clark et al. (2019) opposed and demonstrated that the H I filaments under discussion have enhanced FIR emission in comparison to the H I column densities, implying that this emission must originate from a colder, denser phase of the ISM than the surrounding material. The interpretation in terms of velocity caustics was reinforced by Yuen et al. (2019), but Kalberla & Haud (2020) found it necessary to point out that the small-scale H I and FIR structures under debate are really cold, caused by phase transitions rather than by velocity caustics.

In a recent paper by Yuen et al. (2021), the velocity decomposition algorithm (VDA) is presented with detailed recipes that allow for the separation of the velocity and density contributions from the observed channel maps. This decomposition is closely related to VCA and based on the fundamental VCA postulate (Lazarian & Pogosyan 2000, Sect. 6.3.1) that turbulent density and velocity fields are statistically uncorrelated for the case of magnetohydrodynamical (MHD) turbulence. Yuen et al. (2021) used MHD simulations to support the interpretation that intensity fluctuations are caused predominantly by velocity caustics. The VDA paper extends the VCA paradigms and provides (according to the authors) the further theoretical, numerical, and observational foundations for the theory describing the statistics of the velocity caustics. Furthermore, VDA is claimed to increase the accuracy in recovering the 3D velocity spectral indices. In the following, we apply VDA to the observed local H I distribution. Here, we use an observer’s approach to consider whether the velocity and density fields are uncorrelated and statistically independent of each other.

In Sect. 2, we briefly outline the VDA algorithm. Our HI4PI observations and the data reduction are explained in Sect. 3. The average properties of VDA derived velocity and density contributions are discussed in Sect. 4. A derivation of correlation between velocity and density contributions from the HI4PI data in several localized emission regions is given in Sect. 5. We find that noise biases can dilute derived correlations in a systematic way. Such attenuation effects are discussed in Sect. 6. Our results are incompatible with the basic VCA and VDA paradigm asserting that turbulent velocity and density fields are uncorrelated. The resulting controversies are discussed in Sect. 7. The question as to how far discrepant results may be affected by observational limitations is considered in Sect. 8. Our summary is given in Sect. 9.

2. Velocity decomposition algorithm

Here, we give only a very brief introduction to VDA and for a more detailed explanation, we refer to Yuen et al. (2021). The basic postulate is that in the case of MHD turbulence, the density and the velocity fluctuations are statistically uncorrelated. Using VDA notations, this is formulated as $\langle p_v p_d \rangle = 0$, for an ensemble average indicated by $\langle \dots \rangle$. The observed channel map, p , (usually termed brightness temperature T_B) is decomposed into its velocity contribution, p_v , and density part, p_d , according to:

$$\begin{aligned} p_v &= p - (\langle pI \rangle - \langle p \rangle \langle I \rangle) \frac{I - \langle I \rangle}{\sigma_I^2} \\ p_d &= p - p_v \\ &= (\langle pI \rangle - \langle p \rangle \langle I \rangle) \frac{I - \langle I \rangle}{\sigma_I^2} \end{aligned} \quad (1)$$

with $I = \int p(v) dv$ the total H I intensity (or column density) along the line of sight and $\sigma_I^2 = \langle (I - \langle I \rangle)^2 \rangle$. The necessary condition is that the velocity width Δv of the PPV channel map is small in comparison to the effective velocity width of the observed H I gas. In the following, we use $\Delta v = 1 \text{ km s}^{-1}$, which is adequate to resolve the extraordinarily cold H I cloud with a Doppler temperature of 21.9 K, as observed by Knapp & Verschuur (1972) and sufficient for this kind of analysis. We consider only H I emission structures and exclude strong absorption against continuum background sources. It is important to note that VDA velocity fluctuations are noticeable only in narrow velocity intervals but they vanish if velocity slices get thicker, namely, with $p_v = 0$

for $\Delta v \rightarrow \infty$. Per definition, VDA density fluctuations scale as $p_d \propto I$, particularly for low sonic Mach numbers $M_s \ll 1$ (Yuen et al. 2021, Sect. 3).

3. Observations and data reduction

We used the HI4PI observations (HI4PI Collaboration et al. 2016), combining data from the Effelsberg-Bonn H I Survey (EBHIS, Winkel et al. 2016) that were measured with the Effelsberg 100-m telescope together with data from the revised Galactic all sky survey (GASS, Kalberla & Haud 2015) measured with the 64-m Parkes radio telescope. Retaining the original resolution for each of the telescopes (14.5 for the GASS and 10.8 for the EBHIS), the H I data from both surveys have been gridded to independent $n_{\text{side}} = 1024$ HEALPix databases.

Subsequently, all H I profiles were decomposed into Gaussian components (Haud 2000 and Kalberla & Haud 2015). From the frequency distribution of the velocity dispersions of the Gaussian components, we used the methods of Kalberla & Haud (2018) to distinguish three separate linewidth regimes corresponding to the cold, the warm, and the unstable lukewarm neutral medium (CNM, WNM, and LNM). For a detailed description of the data processing and derivation of power spectra, we refer to Kalberla & Haud (2019).

We used Galactic H I PPV emission data with radial velocities that are corrected for the motion of the local standard of rest; thus, the observer is co-rotating with the Milky Way disk and we assume that the H I gas observed in this velocity frame is a valid probe of the turbulent ISM around us. This assumption is only strictly valid for the local gas distribution in high Galactic latitudes ($|b| > 20^\circ$) and at low velocities (Kalberla & Haud 2019, Sect. 5.8). The velocities of H I observed close to the Galactic plane can be seriously affected by differential Galactic rotation, therefore we omitted such data. Here we consider the velocity range $-25 < v_{\text{LSR}} < 25 \text{ km s}^{-1}$ which appears to be a good complete probe of the local gas that is mostly unaffected by gas at high and intermediate velocities and located at large distances (e.g., Wakker & van Woerden 1997 and Röhser et al. 2016). We draw our conclusions based on the high-latitude gas, but we show, in a few cases, the results from the all-sky distribution. These may be affected by confusion, but we intend to demonstrate that the high-latitude results are most probably representative also all-sky.

4. All-sky maps and average properties

In the following, we use HI4PI brightness temperatures to derive velocity and density contributions according to Eq. (1). Next, we discuss the properties of these p_v and p_d distributions in comparison to MHD simulations discussed by Yuen et al. (2021).

The H I emission is dominated by filamentary structures. On average, the velocity distribution is slightly asymmetric and peaks at $v_{\text{LSR}} = 1 \text{ km s}^{-1}$ (Kalberla et al. 2016). Figure 1 shows in the top left panel the all-sky distribution of the observed H I brightness temperature in a single channel with $\Delta v = 1 \text{ km s}^{-1}$ at $v_{\text{LSR}} = 1 \text{ km s}^{-1}$. At this velocity, the emission is quite strong and T_B reaches a peak temperature of almost 150 K. We compare the observed T_B distribution with the derived velocity and density distributions, p_v and p_d , according to Eq. (1). In addition, we display the orthogonality relation, $p_v p_d$, for the purposes of comparison with the findings of Yuen et al. (2021, Sect. 3, property 1). The latter (discussed in Sect. 5 in more detail) serves as a basic test for the VDA condition, $\langle p_v p_d \rangle = 0$, which was one of

the postulates for the derivation of Eq. (1). The most obvious feature in Fig. 1 is that the p_v and p_d distributions are very similar, except for an inverse scaling (or color bar). The p_v distribution resembles the T_B distribution, however, a visual comparison between T_B and p_v gives the impression that the p_v distribution is somewhat more diffuse. In consequence (discussed in Sect. 7.3 in more detail), the power distributions between spatial frequencies differ. Remarkable is that the p_v distribution is negative over large areas. This result affects the interpretation of velocity caustics. The VDA paradigm is that velocity crowding causes structures that are erroneously interpreted as density effects. Usually, it is only positive caustics that are discussed, but we need to take into account that caustics generate also negative structures. This fact poses a challenge for previous high-resolution interferometer investigations on self-absorption from cold H I (e.g., Esquivel et al. 2003 contra Gibson et al. 2000 and Wang et al. 2020). Moreover, the p_d distribution shows significant negative outliers in the Galactic plane, which is also very unexpected based on comparisons to the observed T_B distribution. The orthogonality display, $p_v p_d$, (see Fig. 1 lower right panel) replicates structures seen in the p_v and p_d displays, indicating that the velocity and density fields are correlated.

To determine the velocity dependence of the orthogonality relation, we calculate $\langle p_v p_d \rangle$ for the range between $-25 < v_{\text{LSR}} < 25 \text{ km s}^{-1}$. Figure 2 indicates that velocity and density distributions at velocities close to 0 km s^{-1} show the strongest deviation from the expected $\langle p_v p_d \rangle \sim 0$. As made clear in Fig. 1, $p_v p_d$ is strongest in the Galactic plane.

A critical parameter in MHD simulations is the sonic Mach number, namely, the ratio between the line-of-sight velocity and the sonic speed. From a Gaussian decomposition, the internal dynamics of the H I distribution, characterized by the velocity dispersion of H I clouds at the observed radial velocities, can be described by the distribution of the harmonic mean Doppler temperatures T_D . The distribution of $\log T_D$ is shown in Fig. 3 and its shape is compellingly similar to that in Fig. 2. The minimum of $\langle p_v p_d \rangle$ is at the velocity where we find the lowest Doppler temperatures. The relation $T_D = 21.86 \Delta v_{\text{eff}}^2 = 121.3 \delta v_{\text{eff}}^2$ can be used to estimate the mean effective full width at half maximum (FWHM) velocity width Δv_{eff} or the corresponding dispersion δv_{eff} of the H I, including thermal and turbulent contributions. Close to zero velocities, this dispersion is 4 km s^{-1} , but increases to 9 km s^{-1} in the wings. The dispersions are critical and characteristic for VDA at various sonic Mach numbers (later discussed in Sect. 7.2).

5. Normalized covariance coefficients

The $\langle p_v p_d \rangle$ distribution, shown in Fig. 2, is obviously inconsistent with the assumption of $\langle p_v p_d \rangle = 0$; however, clear criteria regarding whether such deviations are significant or not are missing. According to Yuen et al. (2021), the normalized covariance coefficient,

$$NCC(A, B) = \frac{\langle (A - \langle A \rangle)(B - \langle B \rangle) \rangle}{\sigma_A \sigma_B}, \quad (2)$$

is a better way to characterize correlations between two 2D maps A and B . Here, we use the same notations as Yuen et al. (2021). This measure, also known as Pearson product-moment correlation coefficient, is scale-invariant and results in $NCC(A, B) \in [-1, 1]$. The case $NCC(A, B) = 0$ implies that the two maps are statistically uncorrelated. A perfect correlation requires that $|NCC(A, B)| = 1$; the sign reflects the slope of the linear regression that can be fitted in this case. Results from Eq. (2) can

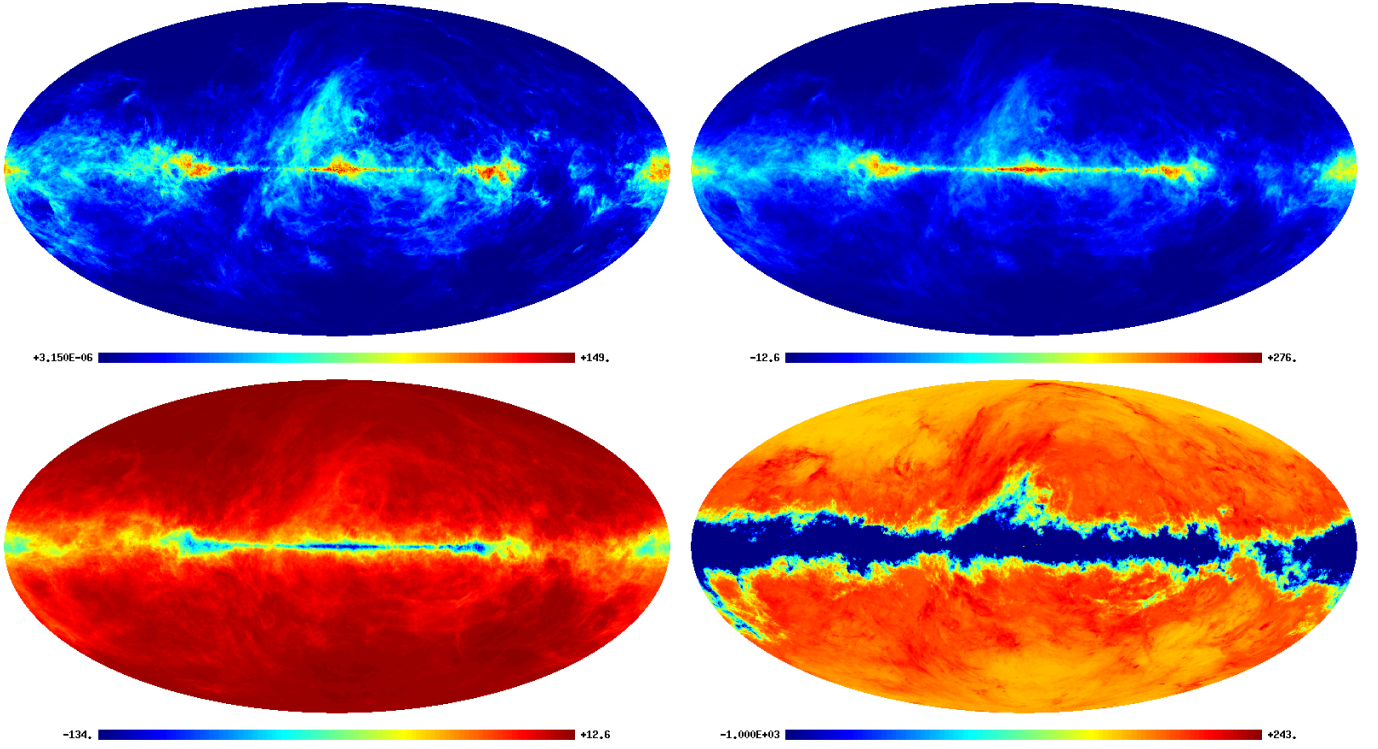


Fig. 1. All-sky Mollweide displays for a single channel at $v_{\text{LSR}} = 1 \text{ km s}^{-1}$. Top left: Observed brightness temperature. Top right: Derived velocity field, p_v . Bottom left: Derived density field, p_d . Bottom right: Orthogonality relation, $p_d p_v$, for p_d and p_v . The minimum for $p_d p_v$ was set for display purposes to $-1\,000 \text{ (K km s}^{-1})^2$; for the other panels, the scale is adopted to the full data range and units are in K km s^{-1} .

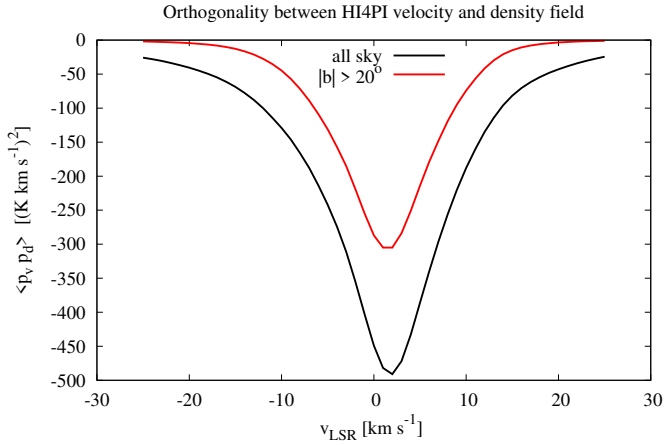


Fig. 2. Orthogonality relation $\langle p_v p_d \rangle$. The red line shows the high galactic latitude sky while the black one shows the all-sky data.

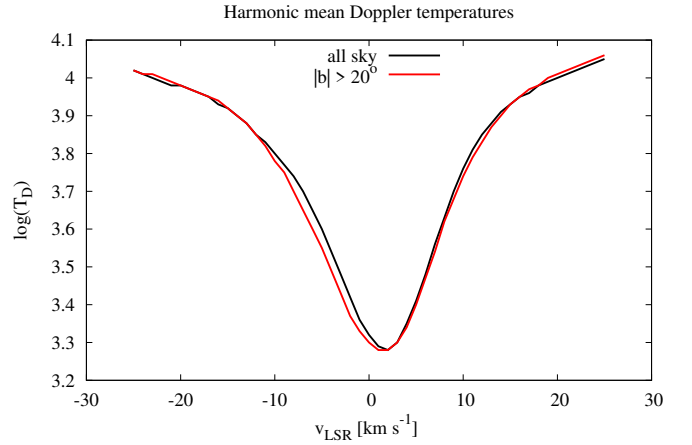


Fig. 3. Harmonic-mean Doppler temperatures for the observed brightness-temperature distribution.

be used to classify the strength of a correlation. A correlation is considered usually as strong for $|NCC(A, B)| > 0.7$, while $|NCC(A, B)| < 0.3$ indicates a weak correlation. Our PPV data cubes contain 51 channels. In the case of a negligible correlation, NCC values around zero with a changing sign are expected, but for a significant correlation, we demand the same sign at all velocities. In the following, we apply the correlation analysis to VDA velocity and density contributions and use the abbreviation $NCC = NCC(p_v, p_d)$.

The statistical properties of velocity and density fields have been discussed by Yuen et al. (2021) for MHD simulations but also for a few selected areas with observational data. Here, we intend to compare their analysis of the GALFA-H I fields

with HI4PI data. For two of the fields the field sizes are $8^\circ \times 8^\circ$, the field centers are located at $\text{RA} = 228^\circ$, $\text{DEC} = 18^\circ 35'$ and at $\text{RA} = 4^\circ$, $\text{DEC} = 10^\circ 35'$. The third field has the boundaries $195^\circ < \text{RA} < 265^\circ$, $19.1^\circ < \text{DEC} < 38.7^\circ$. Yuen et al. (2021) apply VDA in addition to GALFA-H I observations of the high velocity cloud HVC186+19–114. We did not consider this case, since the metallicity and dynamics of infalling decelerated H I clouds are most probably very different from the physical state of the local ISM (Wakker & van Woerden 1997). Here, we considered only H I in our local vicinity. We used HI4PI multiphase H I data decomposed according to Eq. (1) in velocity and density contributions to determine $NCC(p_v, p_d)$. These calculations were repeated for individual H I phases, using CNM, LNM, and

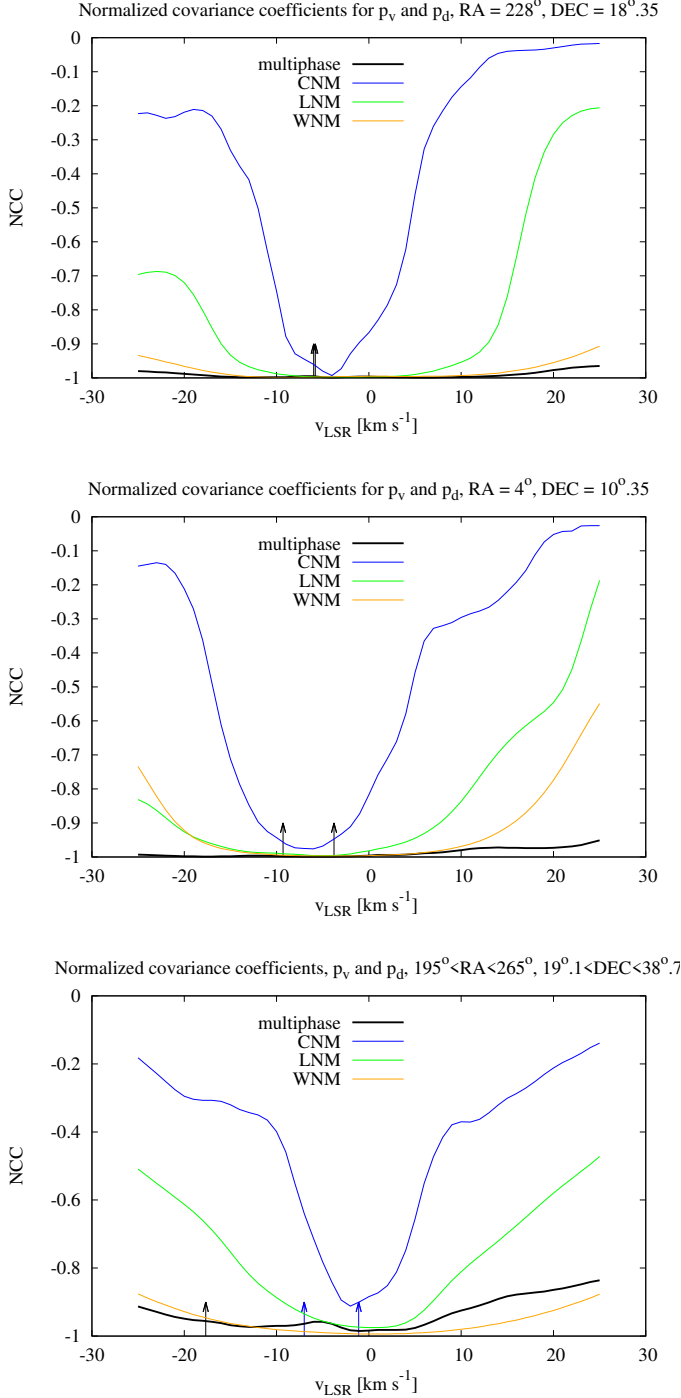


Fig. 4. Normalized covariance coefficients derived from HI4PI data for the multiphase medium as well as separately for the CNM, LNM, and WNM. Two localized $8^\circ \times 8^\circ$ regions are selected. Center positions are $RA = 228^\circ$, $DEC = 18^\circ35'$ at top and $RA = 4^\circ$, $DEC = 10^\circ35'$ in the middle panel. For the bottom panel, the field boundaries are $195^\circ < RA < 265^\circ$, $19^\circ1' < DEC < 38^\circ7'$. The black arrows indicate radial velocities that have been used by Yuen et al. (2021) for discussion. Blue arrows indicate velocities chosen by (Clark et al. 2014).

WNM data from Kalberla & Haud (2015). In each case, we calculated the normalized covariance coefficients $NCC(p_v, p_d)$, shown in Fig. 4. In their examples, Yuen et al. (2021) selected a few velocities only, which are marked in Fig. 4 with black arrows.

All localized emission regions with all individual phases that we considered result in $NCC(p_v, p_d) < -0.9$ at velocities close to the peak emission. The correlation between density and velocity components is evident and consistent close to the line centers, but the velocity wings show a transition towards $NCC(p_v, p_d) \sim 0$. This effect is most prominent for the CNM, in particular for the $RA = 228^\circ$, $DEC = 18^\circ35'$ field at $v_{LSR} \gtrsim 10$ km s $^{-1}$ (Fig. 4, top).

Yuen et al. (2021) demonstrated, using MHD simulations, that the contribution of fluctuations from velocity caustics is maximized in the profile wings. This is considered a key result of their analysis, which allows the applicability of the original VCA technique to be extended by increasing the accuracy in recovering the 3D velocity spectral indices. In the following section, we intend to discuss the reasons for vanishing correlations between p_v and p_d in the profile wings.

6. Noise, de-correlation, and attenuation

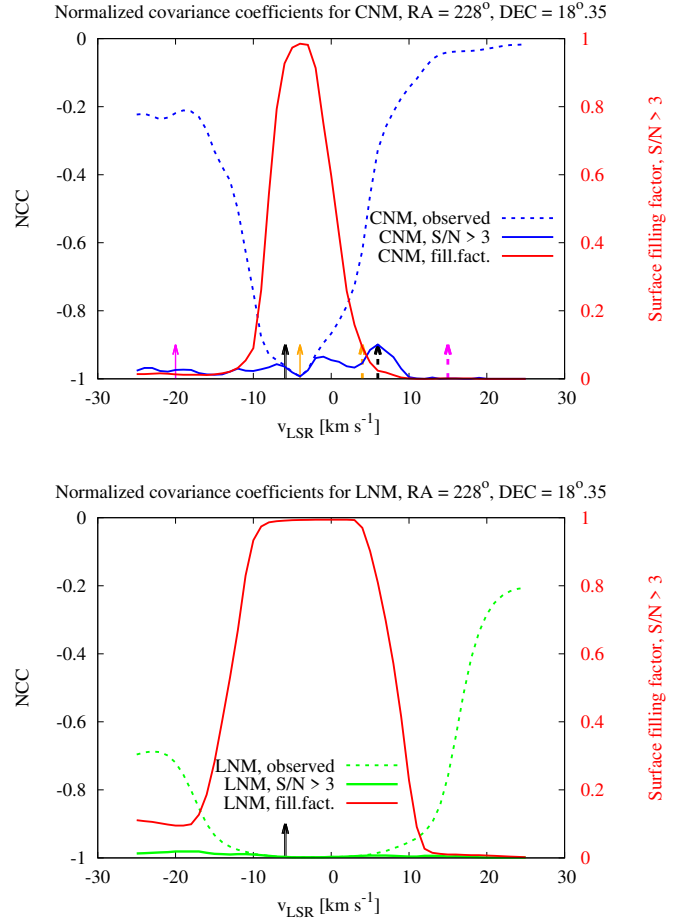


Fig. 5. Normalized covariance coefficients for the CNM (top, blue) and LNM (bottom, green) in the field centered at $RA = 228^\circ$, $DEC = 18^\circ35'$. The solid lines display NCC values from all positions with $S/N > 3$. The dashed lines are the unconstrained NCC values from Fig. 4. The red lines show the surface filling factors for CNM and LNM data with $S/N > 3$. The solid black arrows indicate the radial velocity that was used by Yuen et al. (2021, Fig. 23) for discussion. The other arrows indicate velocities of channel maps discussed in Fig. 6.

It was noted by Spearman (1904) that any correlation between two distributions can be seriously affected by systematic

effects. In the case of a well-defined correlation, the statistical errors necessarily lead to a bias for the derived correlation coefficient. Since contributions from noise are per definition uncorrelated, a pristine correlation is diluted in the presence of noise. [Spearman \(1904\)](#) called this effect attenuation because statistical errors are always attenuating the correlation towards zero¹. In cases where the statistical errors cannot be minimized by increasing the sample, deviations from the correlation become general or systematic. As a test to ascertain the amount of this attenuation and, thereby, to identify the true correlation, [Spearman \(1904, page 90f\)](#) proposed making two or more independent series of the observations. To avoid human prejudices (*Idola Specus, Idola Tribus and Idola Fori*), these series should be sufficiently independent of one another. We follow Spearman's suggestions to spot noise biases.

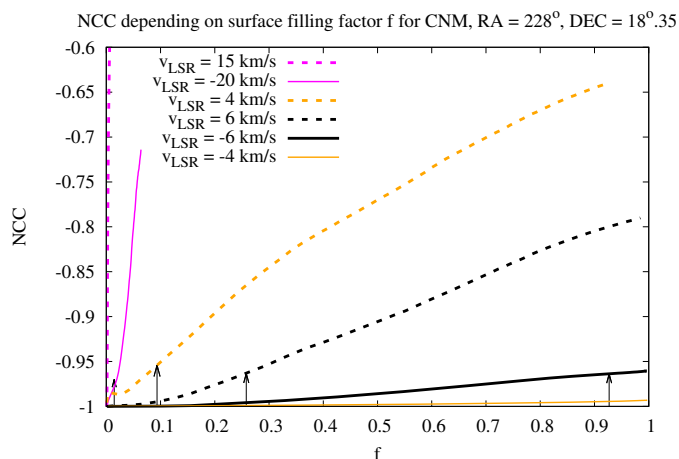


Fig. 6. Normalized covariance coefficients for the CNM in the field centered at RA = 228°, DEC = 18:35 depending on the filling factors obtained by varying the S/N constraint. The arrows point to results for an S/N threshold of three as used in Fig. 5 (top).

6.1. Attenuation effects

In Fig. 4, we find in the top panel for the field at RA = 228°, DEC = 18:35 in case of the CNM at $v_{\text{LSR}} \sim 20 \text{ km s}^{-1}$ that $NCC(p_v, p_d) \sim 0$. A visual inspection of the channel maps in this velocity range indicates that there is barely any observable CNM at $v_{\text{LSR}} \gtrsim 15 \text{ km s}^{-1}$, there is also very little LNM. In this case, the velocity and density contributions for CNM and LNM are spurious, reflecting only unavoidable system noise. This noise component is independent in velocity and position, hence, the uncorrelated and $NCC(p_v, p_d)$ approach zero in this case. Thus, attenuation is expected whenever the noise dominates the observed line signal. The noise dominance depends in general on the signal-to-noise (S/N) ratio.

To distinguish between correlations measured in regions with significant line emission from those regions in position-velocity space that are noise dominated we flag the data at each position and velocity whenever the observed data are below a certain S/N threshold, for most of our discussion we use $S/N > 3$. The unflagged data define a subset of our data that are little affected by noise. The flagged data are disregarded when calculating correlations. The NCC distribution for such PPV subsets

in the RA = 228°, DEC = 18:35 field is shown in Fig. 5. Neither the CNM nor the corresponding LNM data that are restricted to $S/N > 3$ show any evidence for $NCC \gtrsim -0.9$, a clear conflict with Fig. 4 (upper panel). To enable an easy comparison of the results from restricted and unrestricted data we display the values from Fig. 4 with dotted lines. We also plot for comparison the velocity-dependent CNM and LNM filling factor, f_3 , defined as the fraction of pixels per channel that have significant data according to the applied S/N. Here, we use the subscript for f to indicate the applied $S/N > 3$. Only at those velocities where high filling factors for CNM or LNM emission are observed the derived NCC values are unbiased. This is at the peak of the line emission. In the velocity wings towards high velocities the unconstrained NCC values in Fig. 4 are increasingly attenuated when f_3 approaches zero. Noise contributions dominate the observed signal, $NCC \sim 0$ for $f_3 \sim 0$.

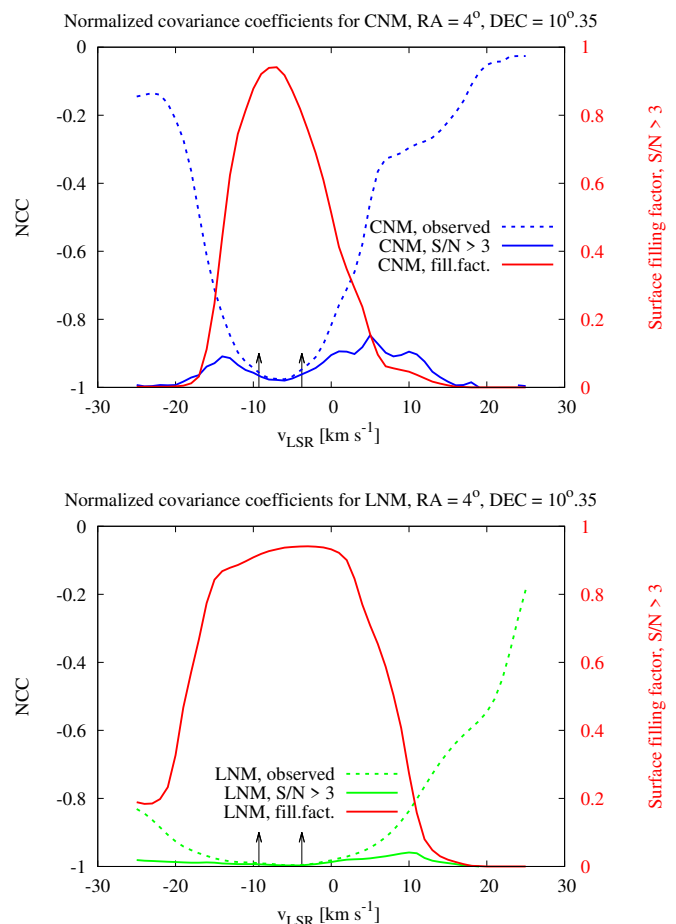


Fig. 7. Normalized covariance coefficients for the CNM (top, blue) and LNM (bottom, green) in the field centered at RA = 4°, DEC = 10:35. The solid lines display NCC values from all positions with $S/N > 3$. The dashed lines are the unconstrained NCC values from Fig. 4. The red lines show the filling factors for CNM and LNM data with $S/N > 3$. The black arrows indicate radial velocity that were used by [Yuen et al. \(2021, Fig. 21\)](#) for discussion.

To verify how far the observed NCC attenuation depends on the filling factor we consider several individual channels at velocities $v_{\text{LSR}} = -20, -6, -4, 4, 6$, and 15 km s^{-1} . For each channel independently we vary the S/N thresholds and determine correlation coefficients NCC and related filling factors f . We obtain, for all selected velocities, monotonic and nearly linear relations

¹ For ISM research this effect is largely unrecognized, searching for abstract keywords “Spearman, attenuation, interstellar medium” delivers no results in ADS

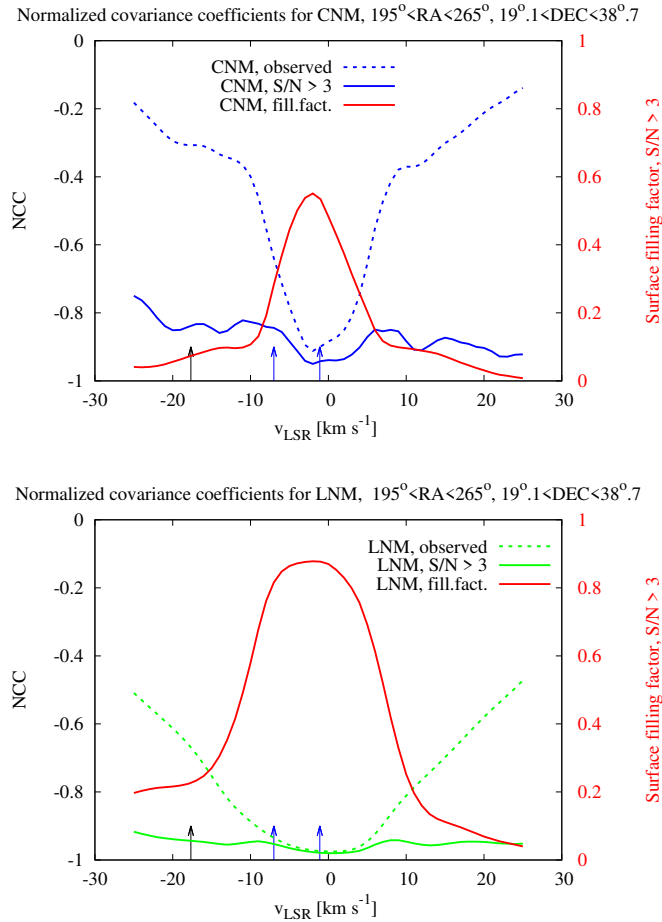


Fig. 8. Normalized covariance coefficients for the CNM (top, blue) and LNM (bottom, green) in the field with the boundaries $195^\circ < \text{RA} < 265^\circ$, $19^\circ.1 < \text{DEC} < 38^\circ.7$. The solid lines display NCC values from all positions with $S/N > 3$. The dashed lines are the unconstrained NCC values from Fig. 4. The red lines show the filling factors for CNM and LNM data with $S/N > 3$. The black arrows indicate radial velocities that have been used by Yuen et al. (2021, Fig. 24) for discussion. Blue arrows indicate velocities chosen by (Clark et al. 2014).

between NCC and f . The slopes of the regression lines shown in Fig. 6 are strongly velocity-dependent. In particular, the edge channels have low filling factors and can be strongly biased by noise. This is easy to understand since significant emission is rather limited in this range. The arrows in Fig. 6 mark NCC and f_3 values determined for $S/N > 3$ as used in Fig. 5. In case of very restrictive high S/N thresholds (left from each arrow) the correlation between p_v and p_d is high but only a small fraction of f within the channel maps may contain such highly significant data. Relaxing the S/N constraints leads to an increase of the filling factors f , in consequence the correlation decreases. Thus, $NCC(p_v, p_d)$ gets systematically attenuated if we release the S/N constraint.

To verify how the observed attenuation depends on the filling factor f_3 for $S/N > 3$ in the other regions, we first considered the field centered at $\text{RA} = 4^\circ$, $\text{DEC} = 10^\circ.35$ (as shown in Fig. 7). Also, in this case there is barely any CNM or LNM emission at $v_{\text{LSR}} \gtrsim 20 \text{ km s}^{-1}$, resulting in a strong attenuation for $NCC(p_v, p_d)$ for unconstrained data. In the case of the field with the boundaries $195^\circ < \text{RA} < 265^\circ$ and $19^\circ.1 < \text{DEC} < 38^\circ.7$, Fig. 8 shows that the filling factors for the CNM and the LNM are

generally well below one. The derived NCC values for CNM are significantly attenuated for $v_{\text{LSR}} \gtrsim 7 \text{ km s}^{-1}$, the density and velocity fields in the velocity wings are clearly correlated in case that H I data with $S/N > 3$ are used.

The exercises discussed above, based on exclusion of noisy data, follow the proposal by Spearman (1904) to consider different subsets of the observed database to spot general or systematic biases. Analyzing several channels in detail we demonstrated in Fig. 6 a systematic attenuation of $NCC(p_v, p_d)$ with decreasing S/N threshold (or increasing filling factor f) in the presence of uncorrelated noise. To get the regressions shown in Fig. 6, we needed a large number of sub-samples by varying the S/N thresholds. We considered only a few of the 51 channel maps and only a single field to demonstrate attenuation effects in detail. These investigations can be extended to other fields and more velocities, we find in any case an improved correlation between velocity and density distributions when S/N restrictions are increased. At the same time, these restrictions lead in all cases to a decrease of the associated filling factor f for the H I distribution used to determine $NCC(p_v, p_d)$.

6.2. HI4PI all-sky data

To generalize our results from individual fields, we went on to consider the all-sky HI4PI data. We apply the same $S/N > 3$ constraint that was used in the previous subsection to calculate all-sky covariance coefficients. The result is shown in Fig. 9 with solid lines. We repeat the calculations and use dashed lines for a display of NCC values that are unconstrained by an S/N threshold. It is obvious that the correlation between velocity and density distributions increases significantly when using only high S/N data. This is the case for all individual phases, but also for multiphase data. In all cases we find strong correlations and the strength could even be increased by using S/N thresholds that are significantly larger than three.

We generalize the results from the previous subsection and conclude that HI4PI data are in general incompatible with the VDA paradigm that velocity and density fields are uncorrelated. Weak correlations in velocity wings are in all cases due to the dominance of noise. Correlation coefficients are only meaningful if significant data are used. The most significant part is close to the line centers. The H I emission ceases in the profile wings and noise takes over at high velocities. This implies an increasing dilution of the correlation coefficients and it is getting increasingly harder to take attenuation into account. Applying an S/N threshold has serious shortcomings. The analysis gets biased. At high velocities an increasing fraction of the H I data is disregarded and only emission peaks are taken into account. The only way out of this dilemma would be to add more observations to achieve a better S/N , but then the systematical limitations can only be shifted to higher velocities.

6.3. Noise properties and the velocity channel differential

To round out the discussion in this section, we note that the observational noise we consider here has a standard distribution with a mean of 0 K, contributing positive and negative amplitudes. Observed intensities in channel maps considered by Yuen et al. (2021) are all positive (see e.g., their Fig. 17, also Appendix E.4). The velocity channel differential $\delta(\log p)/\delta v$, defined by these authors, is supposed to be consistent with Eq. (1) but it traces, according to Yuen et al. (2021), the caustics counterpart of the density distribution up to the velocity wings even more

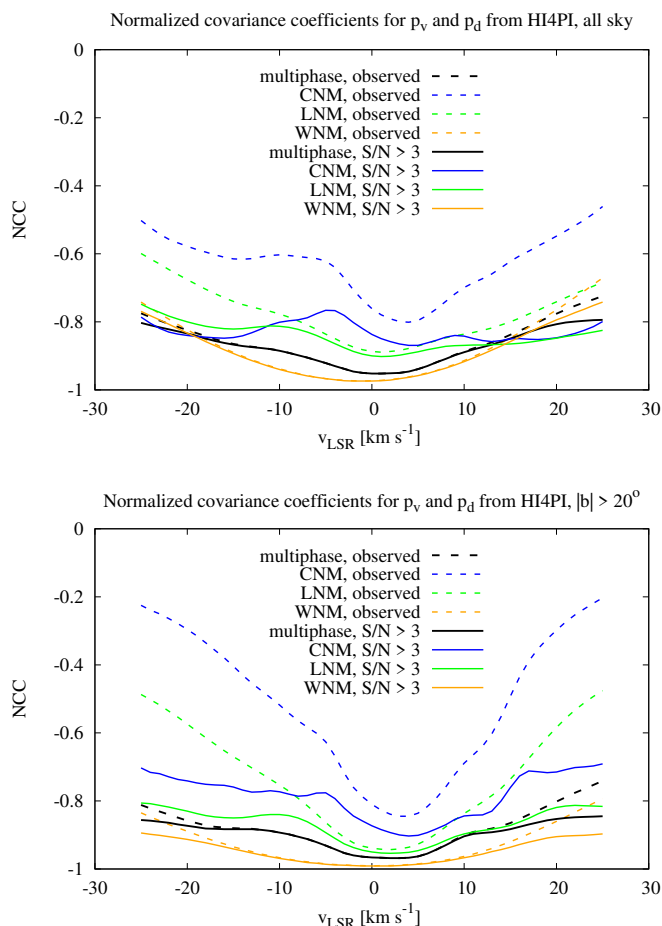


Fig. 9. Normalized covariance coefficients derived from HI4PI data for the multiphase medium as well as separately for the CNM, LNM, and WNM. Data constrained by $S/N > 3$ are shown with solid lines, dashed lines represent data as observed and unconstrained by an S/N threshold. Top: All sky. Bottom: High latitudes only.

accurately than Eq. (1) (see their Fig. 31). These rules are only valid for strictly positive signals; the differential $\delta(\log p)/\delta v$ is not applicable to raw observations that are noisy. In the case of data that are flagged with respect to an S/N threshold (Sect. 6.1), $\delta(\log p)/\delta v$ is applicable. However, in such cases, we observe a strengthening of the correlations between density and velocity fields. Contrary to our results Yuen et al. (2021) report an excellent performance on the part of the velocity channel differential in the case of supersonic MHD simulations under the condition $\langle p_v p_d \rangle = 0$ (property 1 in Appendix E of Yuen et al. 2021).

6.4. Correlations in processed data

We also note that in case of the $195^\circ < RA < 265^\circ$, $19.1^\circ < DEC < 38.7^\circ$ field, the discussion in Yuen et al. (2021) refers to a subset at $v_{LSR} = -17.6 \text{ km s}^{-1}$ with little CNM. At this WNM-dominated velocity, Yuen et al. (2021) applied a rolling Hough transform (RHT, Clark et al. 2015) to the separated velocity and density maps. The resulting linear features shown in Fig. 24 of Yuen et al. (2021) are uncorrelated with $NCC = 0.087$. It is quite unexpected that running an RHT analysis on strongly correlated maps with $NCC(p_v, p_d) = -0.96$ for the multiphase medium (see Fig. 4) would lead to a nearly uncorrelated result with $NCC = 0.087$. In such a case, we

would expect that the resulting RHT maps are also correlated. However, it has been highlighted by (Clark et al. 2014) that the filaments that are aligned with the magnetic field are associated with cold H I. The original RHT analysis by Clark et al. (2014) was done at velocities of $-7 < v_{LSR} < -1.1 \text{ km s}^{-1}$ with a high CNM content, with the velocity range indicated in Fig. 4 with blue arrows. In the interpretation of Clark et al. (2019), the H I filaments originate from the CNM; whereas Yuen et al. (2021) intentionally link the filaments to WNM-dominated regions in high galactic latitudes where the cold phase of H I is known to be subdominant in terms of its mass (Yuen et al. 2019). Both approaches are incompatible and the results are thus not comparable under these conditions.

6.5. Correlations and biases

In summarizing our results, we conclude that the velocity and density fields in the local ISM are strongly correlated, namely, with $NCC < -0.7$. The most significant correlation is found close to the peak emission. Attenuated correlations in the velocity wings of raw data are spurious and caused by systematic de-correlations due to noise. The correlation coefficient that we derive from the HI4PI data is negative at all velocities, while the fluctuations in velocity and density are in general anti-correlated. The implication is that structures in H I channel maps are caused either by density enhancements or by velocity caustics. Our results are in clear contradiction to the MHD simulations and theoretical expectations from uncorrelated velocity and density fields with $NCC \sim 0$.

7. Resolving the controversy

Our result is significant enough that we could end the present publication with the conclusion from Sect. 6.5. However, a few controversies remain, which are described by Yuen et al. (2021) in their Sects. 9.1 and 9.2 and which we intend to clarify in the following.

7.1. Feasibility of distinguishing caustics from density fluctuations

In the literature, the concern lies mainly in whether filamentary structures in H I channel maps are shaped predominantly by velocity caustics or density enhancements. Given that the most prominent H I structures close to velocities of the peak emission show the best defined correlations between VDA velocity and density components, we may conclude that such PPV structures can either be referred to as velocity caustics or density structures. Our results reported above are statistically sufficient to exclude selection effects in position or in phase composition. Considering merely turbulence-induced VDA structures and observationally derived correlation coefficients in the multiphase H I does not allow us to uniquely distinguish between density and velocity effects. The strong observed correlation $NCC(p_v, p_d) \sim -1$ implies that both in the same sense can be correct. This result is, however, in conflict with VCA's key assumption that density and velocity fields are uncorrelated (Lazarian & Pogosyan 2006, Sect. 3 and App. C).

According to Lazarian & Pogosyan (2000), the PPV correlation function can be presented as a sum of two terms, one of which depends on the fluctuations of density, the other does not. Hence, it is possible to separate density and velocity fluctuations (Burkhart 2021). By construction density and velocity

fields are presumed to be homogeneous and uncorrelated (Lazarian & Pogosyan 2006). As far as known, MHD simulations are consistent with this postulate, see Burkhart (2021) for the most recent review. MHD simulations and H I observations are incompatible and allow different interpretations. To bridge the apparent discrepancies, we inspect methodic differences between observations and simulations. The systematical limitations are considered in Sect. 8. As pointed out by Spearman (1904) in the introduction of his paper, the vast majority of our knowledge is only partial. In this sense, we also need to consider more or less pronounced tendencies.

Figure 11 of Yuen et al. (2021) shows that each channel map contains both density and velocity fluctuations for each phase. As discussed in their Sect. 9.2, velocity fluctuations tend to contribute more to the profile's wing channels and the dominance of density fluctuations occurs mostly in the subsonic regime at velocity channels close to the peak emission. Our Sects. 6.1 and 6.2 show that any observational data are limited by noise due to the measurement process. The noise, caused by unrelated background irradiation in real data, significantly affects the low intensity range, namely, the line profile wings. The simulated H I spectra however remain unaffected by such noise biases if thermal noise contributions are absent. While fluctuations in the total column density can arise from density fluctuations on large scales, it has been claimed by Yuen et al. (2021) that even small-scale intensity fluctuations are dominated by velocity caustics, particularly in the velocity wings (see their Figs. 9-19). This general statement is conflict with Clark et al. (2019), Peek & Clark (2019), Kalberla & Haud (2019), and Kalberla & Haud (2020), who interpret H I small-scale structures as having been caused by density enhancements.

7.2. Fluctuations in density and velocity

The relative density and velocity contributions of fluctuations in the channel maps are according to Yuen et al. (2021, Figs. 9 to 15) shaped in a characteristic way. From MHD simulations the dispersions for p_v should be larger than the dispersions of p_d . Furthermore MHD simulations result for the dispersions of velocity caustics as a function of velocity in a double-peak shape. This so called $1-\sigma$ criterion (Yuen et al. 2021, Sect. 6) is proposed for an improved VDA analysis in the profile wings.

We calculated these dispersions for the observed HI4PI multiphase H I and for each of the H I phases individually. Figure 10 reveals that in all cases the fluctuations in p_v are significantly larger than those in p_d . The dispersion curves show some skewness, however, the VDA predicted double-peak structure is not observed. Double peaks for H I gas with an effective velocity width Δv_{eff} were taken from Yuen et al. (2021), and theoretically expected to be separated by $0.95\Delta v_{\text{eff}}$, while their MHD simulations result in a separation of $1.09\Delta v_{\text{eff}}$. From the Doppler temperature distribution of HI4PI data (displayed in Fig. 3), we get with $T_D = 21.86 \Delta v_{\text{eff}}^2$ in the case of the multiphase medium $\Delta v_{\text{eff}} \sim 9 \text{ km s}^{-1}$ at radial velocities close to zero. For the CNM we expect $\Delta v_{\text{eff}} \sim 4 \text{ km s}^{-1}$, for the LNM $\Delta v_{\text{eff}} \sim 10 \text{ km s}^{-1}$ (Kalberla & Haud 2018). There are no indications for peaks at such velocity offsets in Fig. 10.

According to Eq. (17) of Yuen et al. (2021), the velocity field follows a scaling relation, $p_v = p - \langle p \rangle - C(I - \langle I \rangle)$, with a constant C that depends only on radial velocity. From the HI4PI data, we find that C is always positive, peaking at a velocity close to zero. To check how far their Eq. (17) is affecting the dispersions from VDA velocity and density fields, we collapse all derived disper-

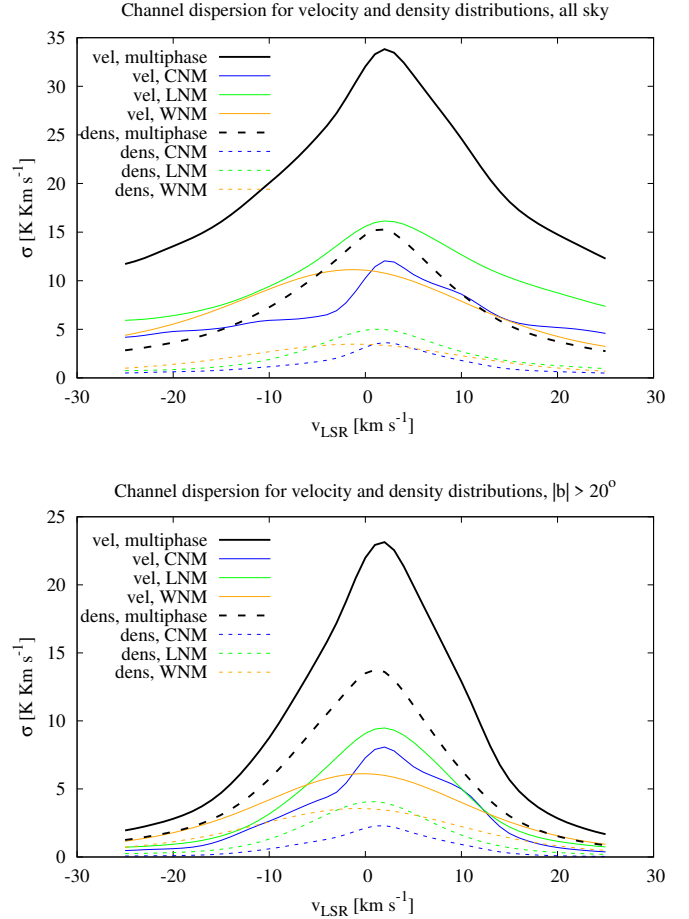


Fig. 10. Channel dispersions for HI4PI density and velocity distributions.

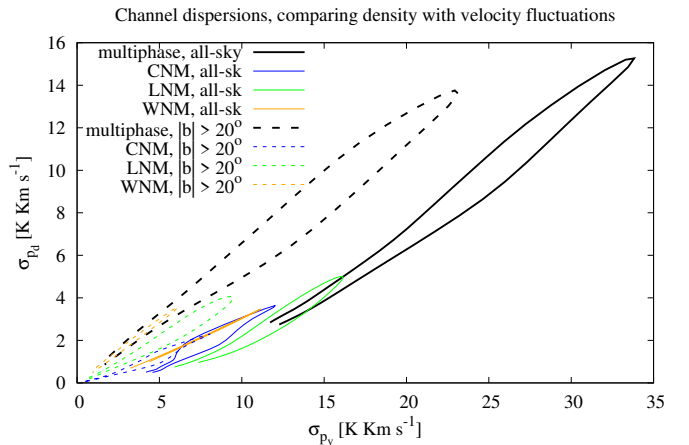


Fig. 11. Channel dispersions derived from HI4PI data, comparing fluctuations in density and velocity.

sions from Fig. 10 into a single diagram. Figure 11 shows that in all cases, $\sigma_{p_v} > \sigma_{p_d}$. Along the loops in this display, we can trace velocity dependences: the upper parts correspond to radial velocities close to zero where the line emission is strongest. Here, the deviation between σ_{p_v} and σ_{p_d} caused by the $C(I - \langle I \rangle)$ term is the greatest, but Fig. 11 shows that the relation between σ_{p_v} and σ_{p_d} is close to linear. This dependence also explains most

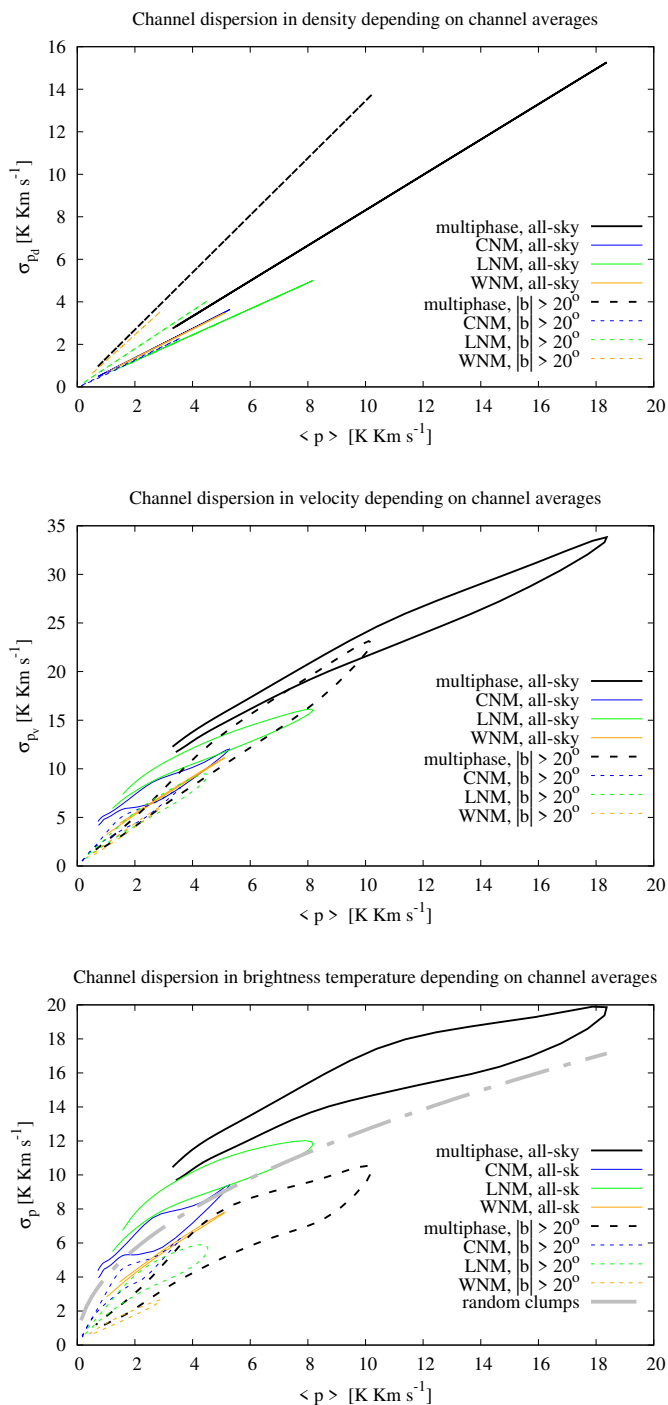


Fig. 12. Channel dispersions depending on average observed intensity from HI4PI data. Top: VDA dispersions p_d in density. Middle: VDA dispersions p_v in velocity. Bottom: Raw dispersions brightness temperatures as observed.

of the expansion of the dynamic range in Fig. 1. While the H I brightness temperatures are limited to 150 K, the caustics cover a range of $-12.6 < p_v < 276$ K at $v_{\text{LSR}} = 0$ km s $^{-1}$. Thus, the velocity fluctuations are artificially scaled up roughly a factor of two with respect to fluctuations in observed brightness temperatures. Considering the dynamical ranges of VDA velocity and density components, we get $(p_{v\text{max}} - p_{v\text{min}})/(p_{d\text{max}} - p_{d\text{min}}) = 2.0$ and that is also the $\sigma_{p_v}/\sigma_{p_d}$ scaling that can be deduced from Fig. 11 at high latitudes.

We would like to comment here also on the relations between channel dispersions and average observed brightness temperatures. The dispersion, σ_{p_d} , for the density field, p_d is, per definition, proportional to $\langle p \rangle$. To verify this relation, we collapse all our data and display the dependences between σ_{p_d} and $\langle p \rangle$ at the top panel of Fig. 12. This plot confirms the linear relation but shows that the scaling constants depend on the selected phases. Below, we display the VDA dispersions from velocity fluctuations, σ_{p_v} ; these also scale in almost a linear way with $\langle p \rangle$. At the bottom of Fig. 12, we display the observed dependence between σ_p and $\langle p \rangle$ without any VDA conversion. These data do not show a linear dependence but they do fit best to a square-root relation, which is expected from the famous [Bienaymé \(1853\)](#) formula for the variance of a sum of uncorrelated random variables. The gray dash-dotted line in this panel with a square-root relation is drawn to guide the eye and it is not a genuine fit. The square-root relation supports the interpretation that observed fluctuations in channel maps are caused by a statistical distribution of real objects (clouds). Dispersions from velocity caustics with a nearly linear scaling do not support such an easy statistical interpretation and the density statistics does even not satisfy the conditions for random variables of a stable normal sequence as considered by [Kolmogorov \(1933\)](#). The contradiction is here that turbulent flows are in general considered to be random but don't follow the law of large numbers for independent and identically distributed sources.

7.3. Power spectra

To determine average scale-dependent fluctuations, we used HI4PI high-latitude data. We calculated the power spectra for the observed brightness temperature distribution, T_B , along with their VDA velocity and density contributions, p_v and p_d . An example is given in Fig. 13, where we selected the radial velocity of $v_{\text{LSR}} = 1$ km s $^{-1}$ because of the well-defined minima in Figs. 2 and 3. All derived power spectra are exceptionally straight and well defined. The density power spectrum (blue) has a power index of $\gamma = -2.93$, within the uncertainties compatible with $\gamma = -2.94$ as determined by [Kalberla & Haud \(2019\)](#). This agreement is remarkable since the value $\gamma = -2.94$ cannot be derived in the VCA predicted very thick velocity slice limit ([Lazarian & Pogosyan 2000](#)) but only for a restricted velocity width of $\Delta v_{\text{LSR}} = 16$ km s $^{-1}$. We refer to the discussion from [Kalberla & Haud \(2019\)](#); in particular their Sect. 5 and their Fig. 14.

The VDA density power spectrum does not depend on the radial velocity except for a general monopole scaling ([Yuen et al. 2021](#), as shown in Eq. (18); see also the discussion in the previous section). The constant shape of the p_d power spectrum implies that the derived p_v power spectrum is velocity-dependent since it is coupled to the T_B power spectrum with observed velocity dependent spectral indices (see Fig. 14, also Fig. 9 of [Kalberla & Haud 2019](#)). The velocity power spectrum that is shown in Fig. 13 is in comparison to the power spectrum from the observed brightness temperature somewhat steeper. Across the analyzed velocity range, we find at high Galactic latitudes, $\gamma(p_v) = \gamma(T_B) - 0.08 \pm 0.02$.

The power spectra from MHD simulations suffer from limitations of the numerical resolution and generally tend to be curved (e.g., [Beresnyak 2014](#), Fig. 1). Observed HI4PI power spectra, as shown in Fig. 13, are far better defined. [Yuen et al. \(2021\)](#) did not present any power spectra from their MHD simulations that could be used for comparison with HI4PI observations. These authors instead used the spectral ratios $P_d(k)/P_v(k)$

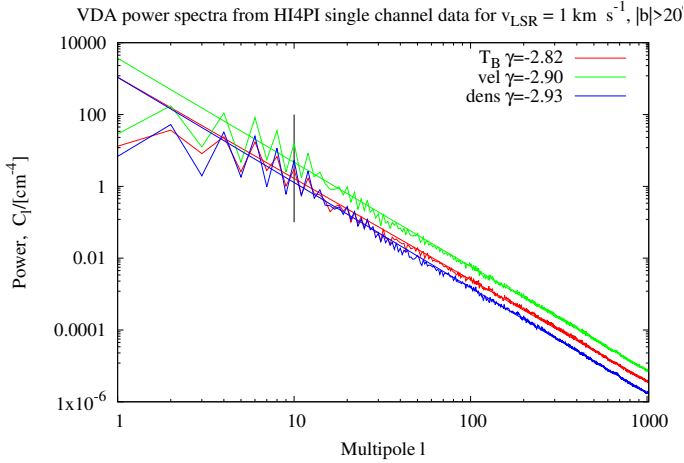


Fig. 13. Power spectra from observed brightness temperatures, T_B (red), velocity contributions, p_v (green), and density contributions, p_d (blue), in a single channels at $v_{\text{LSR}} = 1 \text{ km s}^{-1}$. Spectral indices are fitted, as indicated by a vertical line, for multipoles $l > 10$ only.

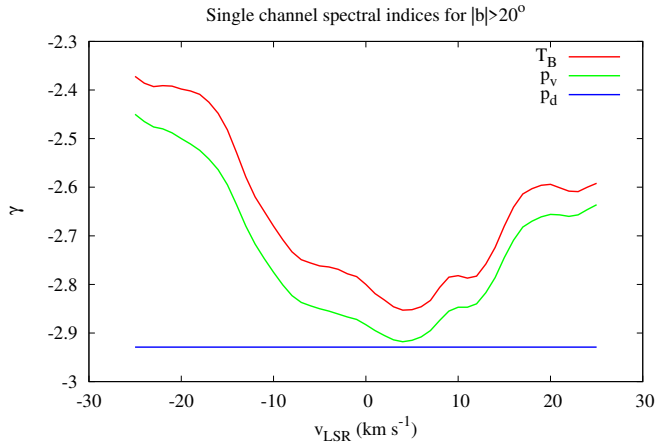


Fig. 14. Velocity dependences of spectral indices derived for observed brightness temperatures and their velocity and density contributions in single channels at high Galactic latitudes.

to distinguish MHD simulations with different sonic Mach numbers (see their Figs. 9 to 11). They find that mostly $P_d(k)/P_v(k) \geq 1$ at the line center but this ratio decreases in the wing channels that Yuen et al. (2021) prefer for their analysis. In contrast, our power ratios $P_d(k)/P_v(k)$ increase as we move away from the center channel (see also Sect. 7.2); in addition, they do not show any peculiarities at wing channels with velocity offsets of $1.09\Delta v_{\text{eff}}$ from the peak emission.

Our Fig. 15 shows the derived power ratios from high-latitude HI4PI data at $v_{\text{LSR}} = 1 \text{ km s}^{-1}$. We plot the ratio $C_l(P_d)/C_l(P_v)$ ² of the derived correlation coefficients for p_d and p_v . In case of the WNM, this power ratio is essentially constant. The LNM shows a slight steepening in the power ratio for $l \geq 100$. This enhancement is more clearly visible for the CNM though these data are somewhat noisier. For the multiphase H I that includes all phases this results in an even more significant steepening of $C_l(P_d)/C_l(P_v)$ towards high multipoles. The multiphase result is independent from any phase decomposition but the CNM, LNM, and WNM power ratios indicate that the steep-

ening of $C_l(P_d)/C_l(P_v)$ at high multipoles is phase-dependent. We would like to point out that power distributions derived from observational data need to be corrected for smoothing from the telescope beam. In the case of power ratios, such instrumental effects, along with their possible associated uncertainties are canceled out. Therefore, the multiphase result is highly significant. As expected, based on McKee & Ostriker (1977) or Wolfire et al. (2003), thermal instabilities cause preferentially cold density condensations on small scales, leading to an increase of $C_l(P_d)/C_l(P_v)$ in this range.

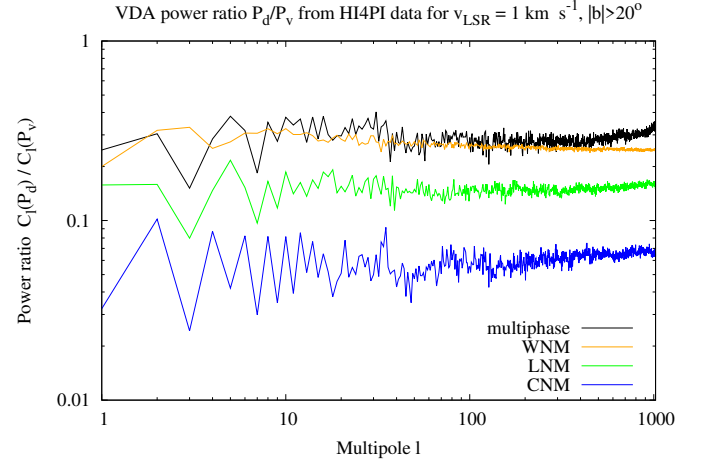


Fig. 15. Power ratio $C_l(P_d)/C_l(P_v)$ between density and velocity fluctuation of the local diffuse H I emission at high Galactic latitudes.

It is clearly useful to compare the multiphase MHD simulations from Yuen et al. (2021, Fig. 11) at a sonic Mach number $M_s = 1.43$ with our results, shown in Fig. 15. In both cases, the ratio $P_d(l)/P_v(l)$ for the WNM does not depend significantly on scale size; Fig. 11 of Yuen et al. (2021) is consistent with our Fig. 15, the WNM distributions are flat in both cases. The unstable LNM shows some discrepancies; the MHD simulations predict, for $P_d(k)/P_v(k)$, a decrease; whereas our data reveal an increase for high spatial frequencies. This opposite behavior between simulations and observations increases for the CNM and further for the multiphase medium (consider the latter case on the basis of Fig. 15 with Yuen et al. 2021, Fig. 10). In agreement with the predictions by Lazarian & Pogosyan (2000), the gradients in $P_d(k)/P_v(k)$ from MHD simulations tend to be steepest for narrow velocity channels, independently of whether center or wing channels are considered. As emphasized by Yuen et al. (2021), their simulations show that turbulence at small scales is increasingly dominated by fluctuations in velocity.

The multiphase MHD simulations, distinguishing CNM, LNM, and WNM, are according to Table 2 of Yuen et al. (2021) obtained at a grid of 480^3 pixels. Higher resolution calculations at a 1200^3 pixel grid are available for $M_s = 0.61$ and 6.36 , but here without a phase decomposition. Figure 9 of Yuen et al. (2021) indicates that for these high-resolution isothermal cases, the trends in the $P_d(k)/P_v(k)$ distributions are quite different from their Figs. 10 and 11 at scales of $k \geq 200$. These deviations remain unexplained and the question arises whether velocity and density power spectra are scale-dependent.

7.4. Linear scales and distances

Our analysis, presented in Fig. 15, applies to multipoles up to $l = 1023$ corresponding to linear scales of about 0.3 pc (Kalberla

² derived using ANAFast from the HEALPix package

et al. 2016). On linear scales lower than 3 pc, equivalent to $l \gtrsim 100$, we observe an increasing $P_d(l)/P_v(l)$ ratio. These linear scales are uncertain but based on the consensus that most of the gas observed at high Galactic latitudes is at a characteristic distance of 100 pc (Clark et al. 2014; Kalberla et al. 2016). A similar distance estimate was given by Lazarian & Yuen (2018, Sect. 11.1). For a typical Kolmogorov type turbulence with a velocity dispersion of 10 km s^{-1} and an injection scale of 100 pc, it is estimated by these authors that on scales larger than 3 pc ($l \lesssim 100$) intensity fluctuations in channel maps are predominantly produced by velocity caustics. The interpretation that filamentary structures observed by Clark et al. (2015) are real physical entities was questioned on this basis by Lazarian & Yuen (2018).

The increase of $P_d(l)/P_v(l)$ in our Fig. 15 on scales below 3 pc is consistent with previous investigations by Kalberla & Haud (2019) and Kalberla et al. (2020). The observed upturn in the power distribution at high spatial frequencies depends on the Doppler temperature of the H I. The power excess (Kalberla et al. 2020, Figs. 14 and 15) for lower Doppler temperatures shifts to higher spatial frequencies. This effect is interpreted with phase transitions that result in the coldest clumps at the smallest scales, which is consistent with Larson (1981). In an approximate pressure equilibrium, the coldest H I structures should be the densest. Assuming further an approximately constant gas-to-dust ratio, the coldest H I structures should also be associated with enhanced FIR emission (e.g., Clark et al. 2019; Kalberla & Haud 2020).

Specifically, VCA applies also to molecular clouds (Burkhart 2021, Table 1). In a recent analysis of the Taurus Molecular Cloud (TMC) by Heyer et al. (2020), it is assumed that structures in thin velocity slices reflect caustics of the turbulent velocity field rather than density fluctuations. The orientations of antenna temperature gradients are compared to the magnetic field orientations, as deduced from Planck 353 GHz polarization data. The authors find that strongly parallel or perpendicular alignments are restricted to localized regions with low levels of turbulence. Zucker et al. (2021) analyzed a sample of 12 molecular clouds, including TMC. They determine molecular gas volume densities using combined data from several surveys (*Gaia*, 2MASS, PANSTARRS, and ALLWISE) that allow for a determination of 3D dust structures. They decompose for all of the analyzed clouds filamentary structures in spines with lower-density outer envelopes and narrow, higher-density inner layers. These density structures are apparently in contradiction with the interpretation of filaments as caustics. We emphasize the importance of distance determinations in their analysis.

A link between structures in the diffuse ISM in H I clouds and the denser molecular clouds is given by Larson's third law, $n \propto L^{-1.1}$ with n as the volume density and L the physical length. Lombardi et al. (2010) point out that this law implies an universal physical structure for clouds with extinctions $A_v \gtrsim 0.1$ mag. This is incompatible with an explanation as caustics. To our understanding filamentary CNM clouds can be considered as objects with a comparable depth to their width on the sky. Distance determination, as emphasized by Zucker et al. (2021) is the key to density structures. Turbulence in the ISM is not scale-free.

8. Limitations

For a comparison between the theoretical and observational results, we need to discuss the question of how far the setup and parameter space in both cases allow for a quantitative comparison. Observations can be limited by instrumental constraints, while MHD simulations may be affected by computational limi-

tations. The huge advantage for simulations is that these can be set up to distinguish parameter spaces that are observationally out of reach. Below, we discuss the constraints on the velocity channel width and Mach numbers.

An essential pillar for VCA is the dependence of observed turbulence properties on the velocity slice thickness. In case of observations we need in particular to consider the limited spectral resolution. The slope of the two-dimensional H I power spectrum changes in a systematic way with the thickness Δv of velocity channel under investigation (Stanimirović & Lazarian 2001, Fig. 1). These authors use H I observations of the Small Magellanic Cloud with a thin channel range for $1.65 < \Delta v < 5 \text{ km s}^{-1}$, a thick channel range for $5 < \Delta v < 22 \text{ km s}^{-1}$, and a very thick range up to 100 km s^{-1} to demonstrate the expected steepening of the derived spectral index. For our analysis, we use a channel resolution of 1 km s^{-1} . GALFA-H I data, considered by Yuen et al. (2021), are available with a channel width of $\Delta v = 0.184 \text{ km s}^{-1}$ (Peek et al. 2018). For MHD simulations at a sound velocity $c_s \sim 0.1 \text{ km s}^{-1}$ Yuen et al. (2021, Fig. 6) apply far higher channel resolutions $0.036 \lesssim \Delta v \lesssim 0.46 \text{ km s}^{-1}$.

A thin velocity channel range of $1.65 < \Delta v < 5 \text{ km s}^{-1}$ was considered to be sufficiently narrow for a VCA analysis by Stanimirović & Lazarian (2001). Below, we work out that we do not expect systematic limitations from a channel width of $\Delta v = 1 \text{ km s}^{-1}$. Haud (2013) studied narrow-line H I emission structures, discussing the detection limits for a Gaussian analysis of particular cold H I clouds with channel widths as low as 0.258 km s^{-1} (Verschuur & Schmelz 1989). Haud (2013) has shown that Gaussian components with widths of $\Delta v_{\text{gauss}} > 0.77 \Delta v$ are reliably detectable. For HI4PI this implies a lower detection limit $T_D \gtrsim 21.86 \text{ K}$ for Doppler temperatures. Extensive H I absorption line studies, summarized by Murray et al. (2018, Fig. 10), indicate that the CNM is ubiquitous. The spin temperature distribution peaks at $T_s \sim 40 \text{ K}$, temperatures below 20 K are sparse and $T_s \lesssim 10 \text{ K}$ is considered to be unphysical. These authors use a channel width of $\Delta v = 0.42 \text{ km s}^{-1}$ with a detection limit $T_s \gtrsim 2.3 \text{ K}$. The spin temperature distribution represents a lower limit to observable Doppler temperatures. In summary, our instrumental setup does not affect the analysis of CNM structures observed in emission towards the diffuse interstellar medium.

A CNM in front of a sufficient strong line or continuum background may be invisible or show up as H I self absorption (HISA) (Gibson et al. 2000) – H I with excitation temperatures below the background brightness temperature causes in any case HISA structures (Wang et al. 2020). These authors summarize (in their Fig. 12) the characteristic properties of such HISA components. Typical FWHM linewidths of the HISA structures are in the range from 3 to 6 km s^{-1} . The frequently associated ^{13}CO emission has line widths between 2 and 4 km s^{-1} . Mach number estimation shows that the ^{13}CO emission is dominated by supersonic turbulent motions, whereas a large fraction of the HISA structures is at subsonic or transonic velocities.

Because of the typical strong background emission, HISA features are easily detectable in the Galactic plane. However, for very cold H I even the cosmic microwave background (CMB) needs to be taken into account. Fluctuations at a channel spacing of $\Delta v \sim 0.036 \text{ km s}^{-1}$ (Yuen et al. 2021, Fig. 6, left panel) imply $T_D \lesssim 0.03 \text{ K}$. This is a subsonic case with $M_s = 0.61$. In the right panel of their Fig. 6 channel maps for $M_s = 6.36$ are shown and we observe a significant fluctuation at a spacing of $\Delta v \sim 0.46 \text{ km s}^{-1}$, corresponding to H I with $T_D \lesssim 4.5 \text{ K}$. Deconvolving this supersonic case for turbulent motions (Heiles & Troland 2003, Eq. (17)), we estimate an H I excitation temperature around $T_e \sim 0.4 \text{ K}$. Thus there are some filamentary structures in Fig. 6 of

Yuen et al. (2021) that are exceptionally cold with $T_e < 2.7$ K. The question arises whether such unphysical structures may be caused by ignoring radiation transport and thermal broadening effects during MHD simulations, see Sect. 3.1 of Clark et al. (2019) for an extended discussion.

Structures shown in Fig. 6 of Yuen et al. (2021) are unexpected and out of reach for traditional H I surveys. For a given observing time τ the system noise ΔT_B , causing brightness temperature uncertainties in individual channels at width $\Delta\nu$, scales as $\Delta T_B \propto 1/\sqrt{\tau\Delta\nu}$. Thus, setting a spectrometer to a channel width of $\Delta\nu = 0.036 \text{ km s}^{-1}$ would require prohibitively long integration times for usual S/N requirements.

The CNM parameter space appears to be most critical if we compare simulations with observations. Yuen et al. (2021, Sect. 4.2) determine a CNM mass fraction of 0.635 for H I with excitation temperatures $T_e < 200$ K. This mass fraction is high in comparison to observational determinations that agree on a CNM mass fraction of about a quarter (Kalberla & Haud 2018; Murray et al. 2018). In case of HI4PI H I emission it is only possible to measure Doppler temperatures and the phase separation is based on a velocity dependent distribution functions, as described in Sect. 2 of Kalberla & Haud (2018). For $v_{\text{LSR}} \lesssim 10 \text{ km s}^{-1}$, the limiting Doppler temperature is essentially $T_D \lesssim 1020$ K. We may compare the HI4PI CNM mass fraction of 0.25 with the fraction of 0.28 determined by Murray et al. (2018). In this case, upper spin temperatures in the range $150 \lesssim T_S \lesssim 350$ K were used to separate the CNM. The link between the distribution of spin- and Doppler temperatures is turbulence with a median turbulent Mach number of about 3.7 (Kalberla et al. 2016). Despite very different observational selection criteria in the emission and absorption observations, there is a surprisingly high consensus about the parameter space covered by the CNM. Our correlations determined in Sect. 5 are independent from the phase composition and therefore we do not expect our conclusion to be affected by uncertainties in the phase fraction.

Yuen et al. (2021) used MHD simulations to discuss Mach number dependencies between VDA structures in velocity and density. Their Fig. 9 (bottom row) shows that density fluctuations dominate velocity caustics on small scales for supersonic turbulence ($M_s \sim 3.49$). As predicted by Lazarian & Pogosyan (2000), this effect is most pronounced for broad velocity channels. The top row of their Fig. 9 shows a subsonic case ($M_s \sim 0.36$). The opposite effect is obvious, velocity caustics dominate with a sharp turn at a scale of $k \gtrsim 1/300$ pixels, independent of the velocity channel width. It is not possible to relate this critical scale to linear or angular scales that are most sensitive for dependencies on Mach numbers. The MHD simulations are however important in the sense that we need to expect a range of high spatial frequencies that is sensitive for a dominance of either velocity or density structures. From H I observations a broad range of Mach numbers is observed for the CNM (Heiles & Troland 2003, Fig. 12) with a median of $M_s \sim 3.7$ (Kalberla et al. 2016). Furthermore, 40% of all components have Mach numbers between 2 and 4 (Murray et al. 2015, Fig. 4). In fields with an overbalance of high Mach-number structures, density fluctuations tend to be dominant.

MHD simulations may be affected by computational constraints. These calculations are limited by a finite grid size. Beresnyak (2014) discusses resolution issues, comparing resolutions between 1024^3 and 4096^3 with significant discrepancies. Most recently, Federrath et al. (2021) used $10,048^3$ cells, however, Burkhardt (2021, Fig. 4) points out that even these simulations miss the relevant range of Reynolds numbers by more than an order of magnitude. It is unclear how serious these limita-

tions are, but it needs to be taken into account that the Yuen et al. (2021) calculations with 480^3 to 1200^3 pixels are low-resolution simulations.

9. Summary and discussion

Applying VDA (Yuen et al. 2021) as an extension and generalization of VCA (Lazarian & Pogosyan 2000) allows us to disentangle fluctuations arising from turbulent velocity and density fluctuations in PPV datasets. The basic underlying assumption is that density and velocity fields are uncorrelated. Yuen et al. (2021) decomposed observations and MHD simulations into velocity and density contributions. They verified the validity of their approach with various MHD simulations for low and high sonic Mach numbers. In general, it is claimed for $M_s < 4$ that VDA velocity and density fields are uncorrelated. Correlation coefficients are distributed closely around zero, typically with $|NCC(p_v, p_d)| \lesssim 0.15$, but also in a few cases approaching $|NCC(p_v, p_d)| \sim 0.3$ (Yuen et al. 2021, Fig. 26). Comparing the decomposed VDA velocity caustics, p_v , with initial caustics, n , from simulations in case of constant density channel maps yields the expected strong correlation with $|NCC(p_v, n)| \gtrsim 0.8$ for $M_s < 1$. This correlation weakens only when increasingly supersonic cases are considered but for $M_s \lesssim 4$ still $|NCC(p_v, n)| \gtrsim 0.55$ is obtained (Yuen et al. 2021, Fig. 29). Given this constraint, VDA was proven to be a safe decomposition algorithm.

In addition to isothermal models, Yuen et al. (2021) considered a multiphase medium, containing CNM, LNM, and WNM. These authors conclude that in thin velocity channels the contributions from velocity caustics dominate at small scales and claim that VDA allows for the direct investigations of the turbulent velocity field in spectroscopic observations. Here, we use HI4PI observations to check the applicability of this analysis.

We applied VDA to HI4PI all-sky H I observations and study also a few localized emission regions that were considered by Yuen et al. (2021). In all cases we find for VDA derived velocity and density contributions a strong and well defined correlation. This includes multiphase data but also the decompositions into CNM, LNM, and WNM. As noted by Spearman (1904) any correlation between two distributions can be seriously affected by systematic effects. The most significant correlation is found close to the peak emission. Weak correlations at velocity wings are spurious and caused by attenuation effects from random noise. We demonstrate that H I observations can suffer in the velocity wings from uncorrelated thermal noise that attenuates an existing correlation. Normalized covariance coefficients depend in this case on the filling factor for those parts of the data that are considered to be significant with respect to the applied S/N threshold. Taking into account that observations at velocity wings and high velocities are increasingly affected by noise, we find no evidence for a genuine de-correlation of density and velocity fields in this range. Our analysis, valid for a velocity channel width of 1 km s^{-1} , results in a general very strong correlation between velocity and density fields that is incompatible with the VCA and VDA paradigm that density and the velocity parts are statistically uncorrelated for the case of MHD turbulence. The analysis by Yuen et al. (2021) covers channel widths as low as 0.036 km s^{-1} . H I survey data at such a high resolution are not feasible because of observational constraints.

Our analysis leads to the following result: $NCC < -0.7$ for all of the selected regions and at all velocities in a negative correlation between velocity and density fields. A negative correlation between two variables means that if one of the variables increases, the other needs to decrease, and vice versa. Figure 1

clearly shows such an anti-correlation between p_v and p_d , in this case $NCC(p_v, p_d) = -0.95$. The negative correlation between p_v and p_d implies that structures in H I channel maps must be caused preferentially either by velocity or density fluctuations.

The observed properties of the H I distribution ought to have a physical background and the physical processes in the ISM need to explain the observed correlation. The conclusion from a negative correlation is that processes that generate density fluctuations must suppress velocity fluctuations. In a similar way, any plausible processes that generate velocity fluctuations must squash the density fluctuations. In the first instance, we may consider phase transitions. These generate density enhancements and, at the same time, the resulting condensations have reduced velocity dispersions that are incompatible with the velocity spread caused by caustics. Without extending the discussion further, phase transitions can be considered to be the best-suited candidates for satisfying a negative correlation between velocity and density fields. The counter example may be velocity shears driven by strong turbulence. It appears plausible that such processes, in particular, at high Mach numbers, generate enhanced velocity fluctuations, disrupting and depleting the local density structures at the same time. To explain the observed negative correlation, it is certainly necessary to have a more detailed discussion of processes of this kind that can lead to a negative correlation. An extended discussion is beyond the scope of our current contribution. We expect, however, that such processes lead to some kind of balance between the velocity and density fields in the ISM.

Yuen et al. (2021) have claimed that structures in the local ISM are dominated by velocity caustics. In the following, we discuss the question of potential dominance between the velocity or density fluctuations. We confirm the VDA prediction that the dispersions of the velocity distribution usually exceed the dispersions of the corresponding density distributions. This effect depends, however, on the relative scaling between density and velocity components. In relating dispersions to the dynamic range of velocity and density fluctuations, we find no significant preferences for an excess in velocity fluctuations. Dispersions as a global measure for the strength of fluctuations, disregarding scale sizes of individual structures, are not useful for deciding on the prevalence among the velocity or density fluctuations.

In particular, VDA predicts that density fluctuations increase in proportion to the average line intensity. Hence, the fluctuations are not statistically independent but coupled to the total intensity. Our analysis shows that also VDA velocity fluctuations increase almost proportionally to the average line intensity. Contrary to these linear relations, the dispersions of the observed single channel brightness temperature distributions increase approximately proportionally to the square root of the average intensity. Such a relation is expected if the H I distribution can be described in a statistical sense as the sum of uncorrelated random objects (Bienaymé 1853). This result supports the interpretation of H I clouds as density enhancements. Fluctuations that increase in a linear way with total intensity are incompatible with the statistics of a sample of independent and identically distributed sources.

The linear scaling of VDA density fluctuations with average density implies that the power spectra in thin velocity channels are all identical except for a general scaling in total power caused by the monopole term. The HI4PI power spectra for the VDA velocity field in thin velocity channels at a width of 1 km s^{-1} are found to be slightly steeper than the power spectra of the observed brightness temperatures. We observe the following at high Galactic latitudes: $\gamma(p_v) = \gamma(T_B) - 0.08 \pm 0.02$. The spec-

tral index is steepest at velocities with the highest monopole radiation, close to zero velocities. The ratio $P_d(l)/P_v(l)$ is scale-invariant for the WNM but at high multipoles (small scales) we find a power excess that increases with decreasing Doppler temperature, from LNM to CNM. Also the multiphase H I gas, independent of phases determined from a Gaussian analysis, shows a clear increase of $P_d(l)/P_v(l)$ towards high spatial frequencies or scales below 3 pc. In nearly all cases, VDA predicts, depending on the sonic Mach number, the inverse relation.

From theory, the CNM is expected to be concentrated at small scales (e.g., McKee & Ostriker 1977 or Wolfire et al. 2003). Recent observations by Clark (2018) and Clark & Hensley (2019) have shown that H I filaments are coherent structures, indicating ordered polarized emission analogous to the FIR polarization. At small scales, the closest coherence in orientation angles between H I and FIR at 857 GHz is found in narrow velocity intervals (Kalberla et al. 2021), which is contrary to VCA predictions that assume filaments are tied to caustics (Lazarian & Yuen 2018). These results, while they are consistent with our findings here, are in clear conflict with basic assumptions from VCA and VDA stating that turbulence causes random and statistically independent fluctuations in the velocity and density distribution. It is a common experience to observe that random processes cannot be invoked to generate coherent structures.

The discrepancy between theory and observations has far reaching consequences. To understand turbulence in the ISM, observers and many theoreticians have developed fundamentally different model assumptions. The most discrepant case is the understanding of density structures. Based on VCA, and also reinforced by VDA, density structures are assumed to be related to the total column density distribution. The density structures are adjusted to individual channels by scaling in velocity. Thus intensity enhancements in channel maps are assumed not to be restricted to a particular velocity interval but to come from velocity caustics along the line of sight. The VDA paradigm is that the decomposed p_v captures the statistical features of the velocity caustics that are responsible for structures in channel maps. As discussed in Sect. 8, this model may be restricted to very low gas temperatures $T \lesssim 2.7 \text{ K}$ ($c_s \sim 0.1 \text{ km s}^{-1}$) that are inaccessible to observations because of the irradiation of the cosmic microwave background.

Evaluating the zero-temperature correlation function for an isolated cloud to separate velocity and density fields (Lazarian & Pogosyan (2006), discussed in Sect. 7.1) is a simplification that is in conflict with the observations. Panopoulou & Lenz (2020) identify, at high Galactic latitudes, on average 2.5 to 3 clouds per 0.2 square degree pixel as kinetically distinct components of emission. According to the decomposition by Kalberla & Haud (2018), a single WNM component without any additional structures can be found at high latitudes only at 0.03% of all observed positions. On average, 3.5 CNM or LNM cloud structures are detectable along the line of sight. An all-sky average value yields 7 components within $|v_{\text{LSR}}| \lesssim 25 \text{ km s}^{-1}$.

Intensity enhancements in channel maps are found, in most cases, to be constrained not only in position, but simultaneously in velocity to a narrow parameter range. The distribution is not random but clumpy; hence, volume density enhancements are frequently found to be clustered in velocity without the expected spread from caustics. Furthermore, fluctuations in density are prevalently observed at similar radial velocities. This correlation in position and velocity has given rise to the famous raisin pudding model: the clumpy CNM (narrow lines) is embedded in a more diffuse WNM (broad lines). Since the very first approach by Clark (1965) this model was extended considerably in sev-

eral aspects, most notably the extensions by McKee & Ostriker (1977) to three components regulated by supernova explosions in an inhomogeneous environment. High-resolution FIR and H I observations have recently disclosed filamentary structures that are coupled to the magnetic field (Clark et al. 2014 or Kalberla et al. 2016). FIR structures are observed to be related to CNM density enhancements. Such structures, localized in position and velocity space, do not fit the VDA density model that is linked to the total column density. A PPV clustering is one of the preliminaries for a Gaussian decomposition (e.g., Haud 2000; Verschuur 2004; Kalberla & Haud 2018; Marchal et al. 2019, and Riener et al. 2019). The prime examples for structures that are only detectable with high spatial resolution in narrow velocity intervals are tiny-scale atomic structures (TSAS) (e.g., Heiles 1997, Deshpande 2000, and Stanimirović & Zweibel 2018).

The discrepancies in derived correlation coefficients are strong enough to explain all conflicts that came up in recent literature between some of the observers and theoreticians (Lazarian & Yuen 2018; Clark et al. 2019; Yuen et al. 2019; Peek & Clark 2019, and Kalberla & Haud 2019, 2020). Theoretical models can be adapted to observations. However, there is an additional problem; MHD theory of turbulence supports VCA and VDA in the range of low channel widths. MHD simulations that are usually assumed to be scale-free are a crucial component of the current paradigms for dynamics and evolution of structure in the ISM. Numerical simulations of MHD turbulence are considered to be essential for our understanding of the physical conditions. The 3D simulation cubes by Yuen et al. (2021) were obtained from a single-fluid, operator-split, staggered-grid MHD Eulerian code ZEUS-MP/3D by Hayes et al. (2006), which would be expected to be in conflict with observations. Brandenburg & Lazarian (2013) discussed a number of different MHD simulations but emphasize the correct treatment of velocity fluctuations from the turbulent volume to the PPV space. Kandel et al. (2016) extended VCA for studying turbulence anisotropies. We note that all the authors mentioned above support the assumption of $\langle p_v p_d \rangle = 0$.

From our investigations, we cannot argue that MHD simulations are a priori in conflict with H I observations. However, we like to caution against simulations that claim to be consistent with VCA. The consistency between PPV cubes from MHD simulations with observations needs to be proven by considering the correlation between the derived velocity and density fields. It is only recently that Burkhardt (2021) pointed out that MHD simulations and numerical diagnostics tools are crucial for our understanding of structures in the neutral and molecular ISM. To achieve a convergence between theory and observations, we may need either a change in paradigms or (in the context of our discussion in Sects. 7 and 8) a more consistent theoretical treatment of the observational parameter space.

Acknowledgements. We thank the anonymous referee for critical comments that led to an improvement of the manuscript. PK thanks Susan Clark for inspiring discussions. This research has made use of NASA's Astrophysics Data System. EBHIS is based on observations with the 100-m telescope of the MPIfR (Max-Planck-Institut für Radioastronomie) at Effelsberg. The Parkes Radio Telescope is part of the Australia Telescope which is funded by the Commonwealth of Australia for operation as a National Facility managed by CSIRO. Some of the results in this paper have been derived using the HEALPix package.

References

- Beresnyak, A. 2014, *ApJ*, 784, L20
 Bienaymé, I.-J. 1853, *Comptes rendus de l'Académie des sciences Paris* 37, 309–317.
 Boulanger, F. & Perault, M. 1988, *ApJ*, 330, 964

- Brandenburg, A. & Lazarian, A. 2013, *Space Sci. Rev.*, 178, 163
 Burkhardt, B. 2021, *PASP*, 133, 102001
 Cho, J., Lazarian, A., & Vishniac, E. T. 2002, *ApJ*, 564, 291
 Clark, B. G. 1965, *ApJ*, 142, 1398
 Clark, S. E., Peek, J. E. G., & Putman, M. E. 2014, *ApJ*, 789, 82
 Clark, S. E., Hill, J. C., Peek, J. E. G., et al. 2015, *Phys. Rev. Lett.*, 115, 241302
 Clark, S. E. 2018, *ApJ*, 857, L10
 Clark, S. E., Peek, J. E. G., & Miville-Deschênes, M.-A. 2019, *ApJ*, 874, 171
 Clark, S. E. & Hensley, B. S. 2019, *ApJ*, 887, 136
 Deshpande, A. A. 2000, *MNRAS*, 317, 199
 Elmegreen, B. G. & Scalo, J. 2004, *ARA&A*, 42, 211
 Esquivel, A., Lazarian, A., Pogosyan, D., et al. 2003, *MNRAS*, 342, 325
 Federrath, C., Klessen, R. S., Iapichino, L., et al. 2021, *Nature Astronomy*, 5, 365
 Gibson, S. J., Taylor, A. R., Higgs, L. A., et al. 2000, *ApJ*, 540, 851
 Haud, U. 2000, *A&A*, 364, 83
 Haud, U. 2013, *A&A*, 552, A108
 Hayes, J. C., Norman, M. L., Fiedler, R. A., et al. 2006, *ApJS*, 165, 188
 Heiles, C. 1997, *ApJ*, 481, 193
 Heiles, C. & Troland, T. H. 2003, *ApJ*, 586, 1067
 Heiles, C. & Troland, T. H. 2005, *ApJ*, 624, 773
 Heyer, M., Soler, J. D., & Burkhardt, B. 2020, *MNRAS*, 496, 4546
 HI4PI Collaboration, Ben Bekhti, N., Flöer, L., et al. 2016, *A&A*, 594, A116
 Kalberla, P. M. W. & Kerp, J. 1998, *A&A*, 339, 745
 Kalberla, P. M. W., Burton, W. B., Hartmann, D., et al. 2005, *A&A*, 440, 775
 Kalberla, P. M. W. & Haud, U. 2015, *A&A*, 578, A78
 Kalberla, P. M. W., Kerp, J., Haud, U., et al. 2016, *ApJ*, 821, 117
 Kalberla, P. M. W. & Haud, U. 2018, *A&A*, 619, A58
 Kalberla, P. M. W. & Haud, U. 2019, *A&A*, 627, A112
 Kalberla, P. M. W. & Haud, U. 2020, *arXiv:2003.01454*
 Kalberla, P. M. W., Kerp, J., & Haud, U. 2020, *A&A*, 639, A26
 Kalberla, P. M. W., Kerp, J., & Haud, U. 2021, *A&A*, 654, A91
 Kandel, D., Lazarian, A., & Pogosyan, D. 2016, *MNRAS*, 461, 1227
 Knapp, G. R. & Verschuur, G. L. 1972, *AJ*, 77, 717
 Kolmogorov, A., 1933, *Grundbegriffe der Wahrscheinlichkeitsrechnung (Ergebnisse der Mathematik und Ihrer Grenzgebiete. 1. Folge, 2)*, Springer
 Larson, R. B. 1981, *MNRAS*, 194, 809
 Lazarian, A. & Pogosyan, D. 2000, *ApJ*, 537, 720
 Lazarian, A. & Pogosyan, D. 2006, *ApJ*, 652, 1348
 Lazarian, A. & Yuen, K. H. 2018, *ApJ*, 853, 96
 Lombardi, M., Alves, J., & Lada, C. J. 2010, *A&A*, 519, L7
 Marchal, A., Miville-Deschênes, M.-A., Orioux, F., et al. 2019, *A&A*, 626, A101
 McClure-Griffiths, N. M., Pisano, D. J., Calabretta, M. R., et al. 2009, *ApJS*, 181, 398
 McKee, C. F. & Ostriker, J. P. 1977, *ApJ*, 218, 148
 Miville-Deschênes, M.-A., Duc, P.-A., Marleau, F., et al. 2016, *A&A*, 593, A4
 Murray, C. E., Stanimirović, S., Goss, W. M., et al. 2015, *ApJ*, 804, 89
 Murray, C. E., Stanimirović, S., Goss, W. M., et al. 2018, *ApJS*, 238, 14
 Murray, C. E., Peek, J. E. G., & Kim, C.-G. 2020, *ApJ*, 899, 15
 Panopoulou, G. V. & Lenz, D. 2020, *ApJ*, 902, 120
 Peek, J. E. G., Babler, B. L., Zheng, Y., et al. 2018, *ApJS*, 234, 2
 Peek, J. E. G. & Clark, S. E. 2019, *ApJ*, 886, L13
 Riener, M., Kainulainen, J., Henshaw, J. D., et al. 2019, *A&A*, 628, A78
 Röhser, T., Kerp, J., Lenz, D., et al. 2016, *A&A*, 596, A94
 Salpeter, E. E. 1976, *ApJ*, 206, 673
 Saury, E., Miville-Deschênes, M.-A., Hennebelle, P., et al. 2014, *A&A*, 567, A16
 Spearman, C. The proof and measurement of association between two things. *The American journal of psychology* 15, 72–101 (1904)
 Stanimirović, S. & Lazarian, A. 2001, *ApJ*, 551, L53
 Stanimirović, S. & Zweibel, E. G. 2018, *ARA&A*, 56, 489
 Spitzer, L. 1968, *New York: Interscience Publication*, 1968
 Verschuur, G. L. & Schmelz, J. T. 1989, *AJ*, 98, 267
 Verschuur, G. L. 2004, *AJ*, 127, 394
 Winkel, B., Kerp, J., Flöer, L., et al. 2016, *A&A*, 585, A41
 Wakker, B. P. & van Woerden, H. 1997, *ARA&A*, 35, 217
 Wang, Y., Bihr, S., Beuther, H., et al. 2020, *A&A*, 634, A139
 Wolfire, M. G., McKee, C. F., Hollenbach, D., et al. 2003, *ApJ*, 587, 278
 Yuen, K. H., Hu, Y., Lazarian, A., & Pogosyan, D. 2019, *arXiv:1904.03173*
 Yuen, K. H., Ho, K. W., & Lazarian, A. 2021, *ApJ*, 910, 161
 Zucker, C., Goodman, A., Alves, J., et al. 2021, *ApJ*, 919, 35